

AD-A182 940

FINE-SCALE MECHANICAL PROPERTIES OF SLIDING SOLIDS(U)

1/1

LANCASTER UNIV (ENGLAND) DEPT OF PHYSICS

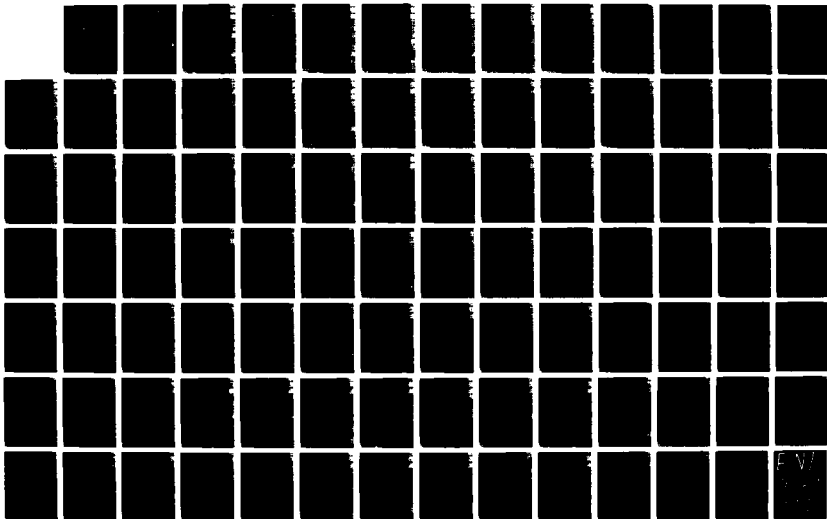
J D ROSS ET AL. 28 FEB 87 R/D-4106-R-AN

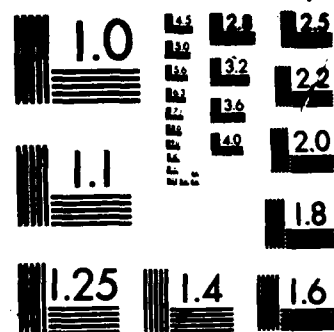
UNCLASSIFIED


DAJA45-84-C-0006

F/G 28/11

ML







 MICROCOPY RESOLUTION TEST CHART

 NATIONAL BUREAU OF STANDARDS-1963-A

AD-A182 940

DTIC FILE COPY

FINE-SCALE MECHANICAL PROPERTIES OF
SLIDING SOLIDS

Final Technical Report

by

J.D.J. Ross and H.M. Pollock

February 1987

United States Army

EUROPEAN RESEARCH OFFICE OF THE U.S. ARMY

London, England

Contract Number: DAJA 45-86-C-0006

University of Lancaster, Department of Physics,
Lancaster LA1 4YB

DTIC
ELECTE
JUL 17 1987
A

Approved for Public Release; distribution unlimited

87 7 16 003

**FINE-SCALE MECHANICAL PROPERTIES OF
SLIDING SOLIDS**

Final Technical Report

by

J.D.J. Ross and H.M. Pollock

February 1987

United States Army

EUROPEAN RESEARCH OFFICE OF THE U.S. ARMY

London, England

Contract Number: DAJA 45-86-C-0006

**University of Lancaster, Department of Physics,
Lancaster LA1 4YB**

Approved for Public Release; distribution unlimited

Unclassified

SECURITY CLASSIFICATION OF THIS PAGE

REPORT DOCUMENTATION PAGE AD-A182940				Approved ON No 0704-0188 Exp Date Jun 30, 1986	
1a REPORT SECURITY CLASSIFICATION Unclassified		1b RESTRICTIVE MARKINGS None			
2a SECURITY CLASSIFICATION AUTHORITY		3 DISTRIBUTION/AVAILABILITY OF REPORT Approved for public release; distribution unlimited			
2b DECLASSIFICATION/DOWNGRADING SCHEDULE					
4 PERFORMING ORGANIZATION REPORT NUMBER(S)		5 MONITORING ORGANIZATION REPORT NUMBER(S) R&D 4106-R-AN			
6a NAME OF PERFORMING ORGANIZATION University of Lancaster		6b OFFICE SYMBOL (if applicable)		7a NAME OF MONITORING ORGANIZATION USARDSG(UK)	
6c ADDRESS (City, State, and ZIP Code) Lancaster LA1 4YB England		7b ADDRESS (City, State, and ZIP Code) Box 65 FPO NY 09510-1500			
8a NAME OF FUNDING/SPONSORING ORGANIZATION USARDSG-UK ARO-E		8b OFFICE SYMBOL (if applicable)		9 PROCUREMENT INSTRUMENT IDENTIFICATION NUMBER DAJA45-84-C-0006	
8c ADDRESS (City, State, and ZIP Code) Box 65 FPO NY 09510-1500		10 SOURCE OF FUNDING NUMBERS PROGRAM ELEMENT NO 61102A			
		PROJECT NO 1L161102BH		TASK NO 57 06	
		WORK UNIT ACCESSION NO			
11 TITLE (Include Security Classification) (U) Fine-scale Mechanical Properties of Sliding Solids					
12 PERSONAL AUTHOR(S) J. D. J. Ross and H. M. Pollock					
13a TYPE OF REPORT Final		13b TIME COVERED FROM 3-12-84 to 2-12-86		14 DATE OF REPORT (Year, Month, Day) 1987, February 28	
				15 PAGE COUNT 91	
16 SUPPLEMENTARY NOTATION					
17 COSATI CODES FIELD GROUP SUB-GROUP 11 08 20 04			18 SUBJECT TERMS (Continue on reverse if necessary and identify by block number) Adhesion, friction, microhardness, ultra-high vacuum mechanical microprobe, sub-micron indentation device, microdeformation, mechanical characterisation.		
19 ABSTRACT (Continue on reverse if necessary and identify by block number) This report describes fine-scale contact experiments specifically designed to investigate the mechanical properties of materials at the submicroscopic level. The first part deals with experiments carried out using an ultra-high vacuum (UHV) mechanical microprobe in which adhesion and friction are measured between a sharply-pointed metal tip and a flat surface at very light loads. The results show that, for a metal-metal or metal-ceramic interface, the adhesion and frictional resistance to tangential sliding are highest for clean surfaces in UHV. However, for contacts between a metal tip and an amorphous metallic glass both adhesion and friction are lower after standard cleaning procedures in UHV. Part II describes fine-scale indentation measurements on thin films and ion-implanted surfaces carried out in the laboratory ambient. It is shown that surface layers less than a few hundred nanometres thickness can be successfully characterised in terms of plastic, elastic and time-dependent properties. (K. J. L. J. S.)					
20 DISTRIBUTION/AVAILABILITY OF ABSTRACT <input checked="" type="checkbox"/> UNCLASSIFIED/UNLIMITED <input checked="" type="checkbox"/> SAME AS RPT <input checked="" type="checkbox"/> DTIC USERS			21 ABSTRACT SECURITY CLASSIFICATION Unclassified		
22a NAME OF RESPONSIBLE INDIVIDUAL Dr. Fritz H. Oertel, Jr.			22b TELEPHONE (Include Area Code) 01-409 4423		22c OFFICE SYMBOL AMXSN-UK-RA

DD FORM 1473, 84 MAR

83 APR edition may be used until exhausted
All other editions are obsoleteSECURITY CLASSIFICATION OF THIS PAGE
Unclassified

18. Contd. ion-implantation, thin films, time-dependent plasticity, fine-scale mechanical properties, surface properties, single asperity contact.

Abstract

This report describes fine-scale contact experiments specifically designed to investigate the mechanical properties of materials at the submicroscopic level. The first part deals with experiments carried out using an ultra-high vacuum (UHV) mechanical microprobe in which adhesion and friction are measured between a sharply-pointed metal tip and a flat surface at very light loads. The results show that, for a metal-metal or metal-ceramic interface, the adhesion and frictional resistance to tangential sliding are highest for clean surfaces in UHV. However, for contacts between a metal tip and an amorphous metallic glass both adhesion and friction are lower after standard cleaning procedures in UHV. Part II describes fine-scale indentation measurements on thin films and ion-implanted surfaces carried out in the laboratory ambient. It is shown that surface layers less than a few hundred nanometres thickness can be successfully characterised in terms of plastic, elastic and time-dependent properties.



Keywords

Adhesion, friction, microhardness, ultra-high vacuum mechanical microprobe, sub-micron indentation device, microdeformation, mechanical characterisation, ion-implantation, thin films, time-dependent plasticity, fine-scale mechanical properties, surface properties, single-asperity contact.

Table of Contents

Lists of illustrations and tables

Preface

Part I

Experiments Using the UHV Mechanical Microprobe

1. Introduction
2. Technical Objectives
3. Description of Apparatus
4. Experimental
 4. 1 Nickel on Nickel
 4. 2 Tungsten on Nickel-Boride (NiB)
 4. 3 Tungsten on Titanium Oxide (Ti₄O₇)
5. Discussion
6. Summary and Conclusions
7. Summary of Plans for Future Experiments

Part II

Characterization of Sub-Micron Surface Layers by Indentation

1. Introduction
2. Aims
3. Description of Apparatus
4. Interpretation of Data and Definition of Parameters
5. The Thin Film or Bilayer Problem

- 5. 1 Experimental
 - 5. 1 1 Specimens
 - 5. 1 2 Results
 - 5. 1 2 2 Hard Films on a Soft Substrate
 - 5. 2 Discussion and Conclusions
- 6. Mechanical Properties of Ion-Implanted Surfaces
 - 6. 1 Boron- and Phosphorus-Implanted Nickel
 - 6. 1 1 Specimens
 - 6. 1 2 Results
 - 6. 1 3 Conclusions
 - 6. 2 Nitrogen-Implanted Titanium
 - 6. 2 1 Specimens
 - 6. 2 2 Results
 - 6. 2 3 Discussion
- 7. Time-Dependent Effects at the Submicrometre Level
- 8. Future Objectives

Illustrations and tables

List of Illustrations and Tables

Part I

Figure 1 Ultra-high vacuum mechanical microprobe

Figure 2(a) Tip assembly and loading device

Figure 2(b) Close-up view of the tip showing principle of friction force measurement

Figure 3 Friction force vs distance for three successive passes of tungsten on titania in air (sliding speed ~ 10 nm/sec)

Figure 4 Friction force/electrical resistance vs distance for tungsten on titania in vacuum (sliding speed ~ 10 nm/sec).

Figure 5(a) Electrical resistance vs normal load for tungsten on titania after heating to $\sim 900^\circ\text{C}$

Figure 5(b) Electrical resistance vs normal load for tungsten on titania after heating and ion erosion

Part II

Table 1 Implantation parameters for boron- and phosphorus-implanted nickel.

Table 2 Numerical data for boron- and phosphorus-implanted nickel.

Table 3 Implantation parameters for nitrogen-implanted titanium.

Figure 1 Sub-micron indentation device

Figure 2 Typical depth/load cycle illustrating loading and unloading curves.

Figure 3 Raw loading and unloading curves obtained for a 150 nm thick nickel film on silicon.

Figure 4 Variation of hysteresis area with maximum load for 150 nm thick nickel film and for silicon.

Figure 5 Variation of the elastic recovery parameter with the plastic indentation depth for nickel films of different thickness and for the silicon substrate.

Figure 6 Variation of the off-load depth with square root of load for nickel films of three different thicknesses and for the silicon substrate.

Figure 7 Variation of the normalized plasticity index with the ratio δ_p/h for nickel films of different thickness and for the silicon substrate.

Figure 8 Averaged off-load depths plotted as a function square root of load for a 266 nm thick niobium oxide film grown on polycrystalline niobium.

Figure 9 Averaged off-load depths plotted as a function of square root of load for non-implanted polycrystalline nickel and a nickel 25% boron implanted layer.

Figure 10 Variation of hysteresis area with maximum load for the nickel - 25% boron implanted layer.

Figure 11 Variation of the normalized plasticity index with the ratio δ_p/h for non-implanted nickel and for nickel implanted with different concentrations of boron ions.

Figure 12 On-load indentation depth as a function of square root of load for unimplanted nickel and for nickel implanted with different concentrations of boron ions at a single energy.

Figure 13 On-load indentation depth as a function of square root of load for unimplanted nickel and for nickel implanted with different concentrations of phosphorus ions at a single energy.

Figure 14 Variation of on-load index (left-hand ordinate) and amorphous fraction (right-hand ordinate) with ion dose for single energy implants.

Figure 15 Depth (left-hand ordinate) and elastic recovery (right-hand ordinate) as a function of load for unimplanted nickel and multi-energy nickel - 25% boron implanted film.

Figure 16 Off-load indentation depth as a function of square root of load for unimplanted nickel and for multi-energy nickel-boron films.

Figure 17 Off-load plasticity index (left-hand ordinate) and elastic recovery parameter (right-hand ordinate) plotted as a function of ion dose for multi-energy nickel-boron films and for nickel-boron electroless films.

Figure 18 Off-load indentation depth as a function of square root of load at small depths for amorphous nickel - 25% boron of thickness 120 nm; amorphous nickel - 25% boron of thickness 300 nm; and amorphized trinickel boride.

Figure 19 Elastic recovery parameter as a function of off-load indentation depth for single crystal trinickel boride; amorphous nickel - 25% boron; amorphised trinickel boride and polycrystalline nickel.

Figure 20 Raw loading and unloading curves with different maximum loads recorded on Ti-50%N.

Figure 21 Hysteresis area (left-hand ordinate) and elastic recovery (right-hand ordinate) as a function of load for unimplanted titanium and titanium implanted with 34% and 50% nitrogen respectively.

Figure 22 Off-load indentation depth plotted as a function of square root of load for unimplanted titanium and titanium implanted with 34% and 50% nitrogen respectively.

Figure 23 Plasticity index, normalised to pure titanium, as a function of off-load indentation depth for different concentrations of nitrogen in titanium.

Figure 24(a) Constand load "creep" plot (depth vs time) for polyethylene terephthalate (P.E.T.).

Figure 24(b) "Viscosity" data (equivalent strain as a function of stress) for P.E.T.

PREFACE

In recent years progress has been made in establishing the principles involved when materials are to be selected for use in particular tribological applications. Furthermore, the mechanical properties of certain types of sliding engineering surface can be improved by novel methods of treatment such as ion implantation [1] or laser glazing [2]. However, the mechanisms responsible for increased wear-resistance, for example, are seldom clear and it is difficult to predict in practice how effective any given combination of material and treatment will be. It has become clear that long-term solutions require considerably more fundamental knowledge than is available at present; in particular, with current techniques used to study the behaviour of macroscopic samples, experimental results involve a statistical average of the behaviour of a large number of sub-microscopic contacts. In addition large-scale experiments are insensitive to the properties of the topmost surface layers, which may have considerable influence on the tribological properties of the "system", regardless of whether they are entirely adventitious or deliberately introduced. Thus, if the many factors affecting wear are to be distinguished and separately assessed, it is necessary to isolate and study individual single asperity contact events.

Our approach has been to design and use two complementary types of mechanical instrument to explore these minute and shallow regions: the first is an *ultra-high vacuum mechanical microprobe* for measuring the adhesive and frictional properties of a well-characterised surface, and the second is a *sub-micron indentation device* used in the laboratory ambient to measure plastic deformation, elastic recovery and time-dependent plasticity. Accordingly this report is divided into two parts. The first describes the UHV microprobe and the preliminary work on adhesion and sliding contact carried out with this instrument; part II deals with fine-scale measurements of plastic deformation and elastic recovery in thin films and coatings. Later it will be seen that, although the UHV microprobe was successfully

completed and tested, the sub-micron indentation work produced the most in the way of quantitative results, and in consequence, all five papers so far published relate to the experiments described in part II. Both the UHV work and sub-micron indentation experiments are being actively continued with the help of financial support from elsewhere.

PART I

EXPERIMENTS USING THE ULTRA-HIGH VACUUM MECHANICAL MICROPROBE

1. Introduction

There are very few research groups within the field of surface science investigating the fundamentals of solid-solid interactions at the single asperity level, but prior to the initiation of this research, a limited amount of information had already emerged. We now know, for example, that many metal-metal combinations adhere strongly together [1, 2, 3] provided that the surfaces are clean. Moreover, in the case of a single asperity brought into contact with a flat metal surface, plastic deformation can occur even for zero externally-applied load [2]. This arises firstly as a result of the intrinsic attractive force between clean metals, secondly because the stresses tend to be high in the vicinity of a very small area of contact and thirdly due to a size effect [4] whereby for very small-scale events, the force *available* for plastic deformation dominates the force required to *initiate* plastic deformation. The effect, which could be important in a range of mechanical situations, had been concealed in earlier experiments by the effects of surface roughness and contamination. These problems were overcome with the help of an ultra-high vacuum (UHV) mechanical microprobe installed at Lancaster in which a sharply-curved point (radius less than one micrometre) was brought into static contact with a flat, well-characterized surface. In the course of these experiments Pollock *et al* [2, 5, 6, 7] studied also the mode of separation of two adhering metal surfaces during unloading. They were able to distinguish between brittle fracture at the interface and gross ductile failure (often within the bulk of one sample). Elsewhere, the influence of contaminant layers on the adhesion of metals has been studied. An example is the work of Pashley and Tabor [8] who showed that two monolayers of oxygen were sufficient to reduce the adhesion of tungsten-nickel contacts by a factor of three. Our understanding of metal-ceramic or ceramic-ceramic interfaces is far less advanced. Indeed, it is not known if clean surfaces of this type adhere

strongly at room temperature or whether thermal activation is required before bond formation can occur. Equally, the influence of contaminant films has not been examined in detail although there is some evidence that small amounts of oxygen can increase the adhesion in metal-sapphire contacts [9, 10].

The above results refer, of course, to static contacts. Of equal interest is the behaviour of materials at the sliding interface. It is surprising that even now, it is often unclear which fundamental mechanisms of friction between engineering surfaces apply at the level of an individual asperity contact. For example, it is not even known whether an interface can offer resistance to a shear stress if the adhesion forces are zero! nor has the purely mechanical problem of a self-consistent calculation of frictional force been solved [11] : in principle this must be able to predict both frictional force and rate of energy dissipation in a particular situation, given the correct relation between three independent factors, namely:

the shear stress at the surface;

the resultant changes in the volume stress tensor; and

the geometrical deformation of the materials (so that, for example, the frictional force is not necessarily in the plane of sliding). Meanwhile, various different but incomplete models of friction have been used in analysis of data obtained with different materials. A list of these models might include the following:

1. Energy-based models:

(1a) Slip line field theories, where the frictional force F is a function of elastic moduli, hardness, and asperity slope angle;

(1b) Heilmann and Rigney's model [12] where F depends on the real area of contact, the work-hardening rate, and the shear stress and strain as functions of distance below the surface;

(1c) Models in which the energy dissipation involves other types of internal friction

(anelastic behaviour), or the vibration of either asperities or interfacial atoms themselves.

2. Variations of the Bowden and Tabor "shearing of adhered junctions" model:

(2a) models in which the shear strength varies with pressure;

(2b) models that take into account the fact that the real area of contact can vary not only as a function of load (either elastically or plastically), but also can be increased (again, either elastically or plastically) by intermolecular attraction between the surfaces. An example here is Kendall's formula for the friction of silica powder [13]:

$$F = \text{const. } Ka^3/r$$

where the contact radius a is given by:

$$P + 2 \left(\frac{3}{2\pi w} Ka^3 \right)^{1/2} = Ka^3/r$$

P is the normal load, F the frictional force, w the work of adhesion, K the appropriate elastic constant, and r the radius of curvature of the powder particle).

3. Models involving true sliding at the interface, without the need for adhesion: it is possible that the sliding of ceramics may sometimes involve this type of process, where chemical bonds across the interface are not easily formed, the interaction being principally van der Waals with perhaps some ionic contribution, i.e weaker than the chemical bonds within the bulk ceramic.

4. Fracture mechanics models in which the frictional force acts only where the asperity surfaces are in static contact, and is determined, for example, by a peeling process. This process could be governed by the thermodynamic work of adhesion, as in the model of Savkoor and Briggs [14]:

$$F = \{6\pi wr (4\pi wr + P)\}^{1/2}$$

or by a critical crack opening factor δ_c together with hardness H and work-hardening coefficient, n , as described by Marx and Feller [15].

$$\text{friction coefficient} = \text{const.} \frac{\delta_c}{n^2 (PH)^{1/2}}$$

It may well be that the sliding of stiff (high modulus) solids may involve processes analogous to some of those recently shown to apply in the case of soft elastomers [16]. For instance, the friction between glass and rubber at low speeds involves the formation of a static bond at the molecular level, which is stretched during the sticking phase "adhesive infinitesimal dragging") until rupture occurs: each rupture is followed by a jump of a few nanometres' distance, this relaxation occurring at a frequency that depends upon the temperature.

2. Technical Objectives

In view of the wide gaps in our knowledge of fine-scale contact events, as discussed in the proceeding section, our broad aim was to contribute to the general understanding of the mechanical properties of solid-solid interfaces. In particular, the objectives of this research were

- (i) to extend the scope of the UHV microprobe experiments to include tangential sliding at the interface. For example, in [6] it had been found that ion implantation tended to reduce the adhesion at a titanium-titanium interface by impeding plastic deformation at the single asperity level. We now planned to be able to make corresponding measurements under conditions of sliding contact in order to observe the effect of ion implantation (and other surface treatments) on frictional resistance as a function of load, contact area, speed of sliding etc.
- (ii) Since in our experiments it is possible to detect changes in surface geometry

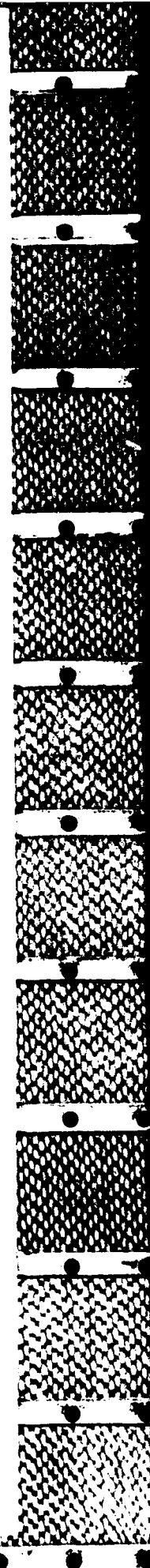
on this scale, we planned to establish the exact mode of deformation of a single asperity during sliding, measuring contact area as a function of load and tangential force, and to investigate transfer of material across the interface. This would allow us to test various models of sliding contact as outlined above;

(iii) to study the influence of contaminant layers on adhesion and friction as a function of the parameters mentioned above.

3. Description of Apparatus

Figure 1 shows the ultra-high vacuum (UHV) chamber and associated instrumentation. The pressure in the chamber (volume $\sim 0.1 \text{ m}^3$) can be maintained at less than 10^{-9} Torr using an ion pump but this can be reduced to around 10^{-10} Torr for definitive experiments by periodic operation of a sublimation pump. This whole system is mounted on a table of large mass and supported on air jacks to minimise the effect of stray vibrations.

Following the work of Pollock *et al* [4, 5], the contacting surfaces consist of a field emitting tip (typical radius 25-250 nm) and a crystal, foil or other flat surface. A close-up view of the tip assembly and loading device is shown in Fig. 2(a). In the experiments to be described, the tip was prepared by chemical polishing or electropolishing and welded to a loop of wire that could be resistively heated in UHV to temperatures approaching the melting point of the tip at currents less than 1.5 A. This in turn was welded to a pendulum supported on near-frictionless indium pivots and incorporating the heating circuit. Preliminary tests showed that no degradation of the pivots would occur using currents of up to 1.5 A. The electrostatic loading system enables positive or negative forces (corresponding to loading and unloading respectively) between 100 nN and 150 mN, with a sensitivity less than 50 nN, to be transmitted across the interface. Before and after contact in UHV, field emission measurements allow the cleanliness, smoothness and curvature of the tip to be quantitatively monitored, together with any damage to its surface

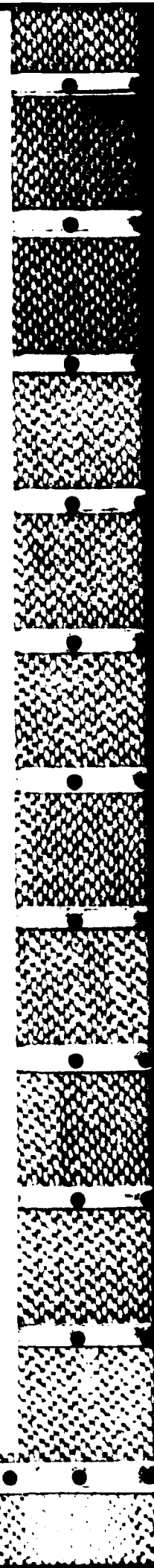


resulting, for example, from ductile failure of an adhesive contact. When the pointed sample is in contact with the opposing surface, the electrical resistance of the contact region is measured as a function of positive and negative load, in order to give information on changes in contact area and adhesion forces.

Regarding the flat sample, cleaning was carried out by one of three methods. Resistive heating was employed if the crystal or foil was electrically conducting and could be sufficiently thinned by electropolishing. In other cases it was necessary to attach the sample to a wire mesh that could be resistively heated itself to high temperatures. Where neither of these methods were appropriate, cleaning was carried out by argon ion erosion. Following a cleaning cycle, the condition of the flat surface (clean or covered with adsorbed gases or residual layers) was usually analysed by Auger electron spectroscopy (AES). It was therefore possible to characterize both the tip (as described above) and the flat sample prior to or following any particular contact experiment.

The sliding contact experiments were designed along the lines of the work previously described by Pollock and Chowdhury [7] in which the flat sample was moved tangentially to the tip using a sensitive motor-controlled micropositioner and any frictional resistance between the tip and the flat was monitored by means of an optical lever. However, other devices, suited to the measurement of small friction forces were considered also. A capacitance circuit, such as that used by Skinner and Gane [17], was rejected on the grounds that the mass of the capacitor plates would have been excessively high together with the fact that they would have been difficult to accommodate using the present tip assembly. The other arrangement considered was that based on a Pixie transducer [18, 19] capable of measuring forces at least as low as $10\ \mu\text{N}$. However, it was thought that the transducer would become irreparably damaged during tip heating and therefore this type of approach was not pursued further.

Figure 2(b) illustrates the principle of operation of the optical lever. The



light source is a helium-neon laser positioned outside the vacuum chamber and directed at the highly reflecting section welded to the tip wire. The reflected beam is focussed onto an optical detector (also outside the chamber) which is sensitive to small changes in position of the beam. To a good approximation, the beam deflection is proportional to the frictional resistance and the sensitivity of the device is of the same order as the electrostatic loading system mentioned above.

4. Experimental

Each set of tests consisted of (a) normal loading and unloading experiments designed to study adhesion and (b) normal loading followed by tangential movement of the flat sample in order to measure frictional resistance. Other parameters of interest such as tip radius, surface cleanliness and chemical composition of the flat sample were monitored where necessary.

We describe below three sets of experiments where different combinations of tip material and flat sample were used.

(i) In the first instance we chose a suitable example of a metal-metal contact involving surfaces that can be obtained in clean, well-characterized form. The experiments provide a convenient reference to work carried out on ion-implanted nickel described in a later section.

4.1 Nickel on Nickel

A nickel tip and a flat, polycrystalline nickel foil were prepared by electropolishing. It is known that metallic surface oxidise rapidly in air which usually reduces the adhesion to an insignificant level. This was confirmed by normal loading experiments in the laboratory atmosphere where the applied load was varied between 1 - 30 μN . Tangential sliding, under the same conditions and at a sliding speed of 20 nm/sec, produced the following results. When very light loads were used, the force resisting tangential movement was generally too small to be detected, and no

changes in electrical resistance, R , during sliding were observed, R remaining at ∞ (open circuit) throughout the experiment. (in later experiments the sensitivity of the friction-measuring device was greatly increased and therefore these experiments should not be compared directly with subsequent ones carried out under similar conditions). For higher loads (greater than about $10 \mu\text{N}$) small fluctuations in frictional resistance, resembling a stick-slip type of motion, were recorded. During the stick phase (duration usually less than 2 seconds), the resistance to motion increased steadily to a point, denoted F_S (the static friction force), where a rapid slip was observed and the friction decreased to a lower value; the surfaces then moved relative to each other at this low value, denoted F_K (the kinetic friction force), until the next stick phase was encountered. Variations in F_K were generally too small to be recorded. No appreciable decrease in R was seen throughout sliding indicating that "clean", metal-to-metal contact had not occurred during these tests. Subsequently a new nickel tip of similar radius was prepared and the experiments were repeated in UHV.

Before contact was made, the tip was heated to successively higher temperatures until a sufficiently clean and smooth end radius was obtained (as evidenced by field emission microscopy). The foil was then degassed at 6-7 Amps. Contact experiments were performed in a vacuum of $1-2 \times 10^{-9}$ Torr. When the surfaces were touched together, R became unstable, fluctuating rapidly between a low value ($\sim 100\Omega - 1k\Omega$) and open circuit; this behaviour continued until the load was increased to a relatively high value ($> 30\mu\text{N}$) at which point R stabilised around $100 - 500\Omega$. In experiments where the low, stable value of R was achieved, the surfaces were separated only after a negative load was applied. If the unloading cycle was commenced prior to attaining a low stable R value, separation occurred at, or close to, zero load.

Several sliding experiments (sliding speed $\sim 10 \text{ nm/sec}$) were then carried out. The results are categorised as follows. At loads less than $\sim 5\mu\text{N}$, the friction

traces resembled the stick-slip motion observed in air, though the mean F_S value was slightly higher. During sliding, open circuit conditions prevailed, except on occasions when the surfaces were not in relative motion (stick-phase), in which case R became unstable and sometimes dropped temporarily to a low values : the slip phase was invariably accompanied by a sharp rise in R . At higher (intermediate) loads, the stick phases became more frequent and prominent, the electrical resistance changes being similar in nature to those above. At the highest loads used ($\sim 30 \mu\text{N}$), F_S was initially large as the tangential motion was applied, after the first slip, however, the observed behaviour was similar to that described for intermediate loads. After completing the preliminary experiments the metal foil became buckled during heating (to remove absorbed gases) and no further experiments were carried out on this specimen.

(ii) As we shall see in Part II, the tribological properties of nickel, e.g. resistance to seizure can be greatly improved by implantation with boron ions. Increases in boron ion concentration are accompanied by progressive amorphization of the surface and complete amorphization occurs when the boron ion concentration exceeds about 22%. At this point, the surface is considerably harder than the original nickel lattice. As described later in Part II, it is thought that surface hardening is a beneficial effect but is not necessarily sufficient to explain the observed changes in tribological behaviour. It was therefore of interest to determine the adhesion and frictional properties of the amorphous layer.

4.2 Tungsten on Nickel-Boride (Ni-B)

The specimen under consideration here was a sample of boron-implanted nickel containing 25% boron ions to a depth of 300 nm. Because of the relatively high hardness of this specimen a tungsten wire, electropolished to a tip radius of $\sim 100 \text{ nm}$, was chosen in preference to nickel in order to reduce the likelihood of irreparable tip damage during contact experiments.

The first contacts, involving normal loading and unloading with a "clean" tip, were carried out in UHV ($\sim 1 - 2 \times 10^{-9}$ Torr) with the specimen in the as-received condition (amorphous Ni-B reverts to a crystalline structure at temperatures greater than about 400°C and a therefore heating of the specimen, to remove absorbed gases, could not be carried out at this stage). Indeed, examination of the surface by AES revealed oxygen and carbon as the principal contaminants. The results were rather variable. Adhesion was found to occur over a wide range of loads although, in general, the force to separate the surface increased with increasing normal load and was higher than that recorded for nickel-nickel contacts in vacuum. Less often, separation occurred at zero load indicating a non-adhesive contact. For separation under adhesive conditions, comparison of field emission images and current-voltage characteristics of the tip before and after contact indicated transfer of material across the interface. In these cases, the original radius of the tip was easily restored by heating following each contact; it was concluded therefore firstly that the tip remained essentially intact throughout the experiment and secondly that material transferred to the tip during unloading.

Tangential sliding under the same conditions produced friction traces similar to those observed for nickel-nickel contacts in vacuum although, for adhesive contacts, the force, F_S , required to break the junction (corresponding to where the slip first occurred) was generally greater. On the other hand, the electrical resistance during sliding was more stable (open circuit); only occasional instabilities were observed (lowest $R \sim 50\text{k}\Omega$) particularly when relatively high loads were used.

A second set of experiments was conducted following argon ion bombardment of the specimen. Chemical analysis of the bombarded surface by AES confirmed the removal of absorbed gases such as oxygen, carbon monoxide etc. It appeared also that preferential sputtering of nickel had taken place during ion bombardment, leaving the surface comparatively rich in boron. Surprisingly, little or no

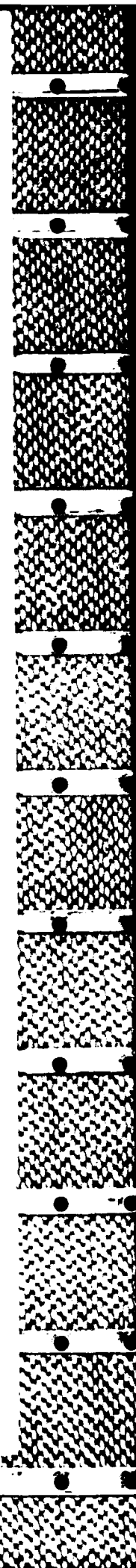
adhesion was observed when the tests were repeated under these condition : this is opposite to the expected behaviour i.e. strong adhesion associated with a clean metal surface. Consequently, in friction experiments, the relatively high initial resistance to tangential movement, F_S , was not observed as before. Friction traces during sliding took the form of rapid stick-slip with a mean F_S appreciably lower than the as-received surface.

(iii) It has already been mentioned that there are few data on the adhesion and friction properties of metal-ceramic and ceramic-ceramic combinations at the single asperity scale. In the following, we describe some recent work on the contact behaviour of a tungsten tip and a conducting ceramic material of industrial interest.

4.3 Tungsten on Titanium Oxide (Ti_4O_7)

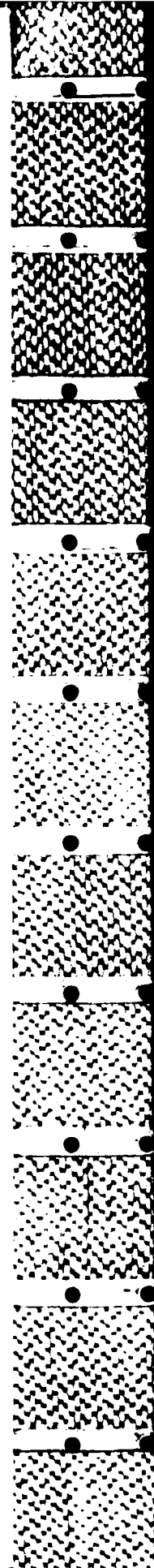
The titania was prepared by ICI in the form of a polycrystalline rod, approximately 15 mm x 3mm x 2mm. Viewed at 500 x magnification in an optical microscope, the surfaces were quite rough and faceted. It could be heated resistively to a temperature (in vacuum) of more than 1000°C at less than 10 A. Initial experiments were carried out in the laboratory ambient. During a typical loading cycle the resistance R became unstable shortly after contact and continued to fluctuate between open circuit and $\sim 10K\Omega$ as the load was increased. Similar behaviour was observed during unloading. Separation of the tip occurred at, or close to, zero load indicating that spontaneous adhesion had not occurred. Tangential sliding, under the same conditions, was characterised by a marked stick-slip movement, and, for repeated traversals over the same regions produced reasonably reproducible traces as shown in figure 3. "Stick" phases were often accompanied by a sudden drop in R , followed by a sharp increase in R during slip as depicted in figure 4.

Corresponding measurements were then carried out in UHV. Before contact



was made, the specimen was resistively heated and analysed using AES. It was found that a clean surface i.e. devoid of residual absorbed gases, could be obtained by heating to $\sim 1000^{\circ}\text{C}$ for five minutes. However, at this temperature, bulk impurities in the titania, notably calcium, phosphorus and sulphur, diffused to the surface. The variation of R with normal load under these conditions is depicted in figure 5(a). It is seen that R drops sharply as the surfaces come into contact, rises to an intermediate value as the load is increased and finally stabilizes (5-10K Ω) at a higher load which varied somewhat from point to point on the specimen. In cases where the load was increased to point A figure 5(a) the surfaces adhered strongly to each other. Sometimes it was found that the force required to separate the tip was greater than the maximum force which could be applied electrostatically and some other means had to be used. If unloading was started before this point was reached, the tip separated at a much smaller negative load. No appreciable changes in R were observed during unloading (prior to separation) indicating failure at the interface by brittle fracture. Field emission microscopy suggested that material had transferred to the tip during these experiments.

Since strong adhesion had been observed under these conditions, it was expected that the frictional resistance to tangential motion would be high after the application of a normal force corresponding to point A in figure 5(a). This was indeed the case. In a number of cases the junction could not be broken by tangential movement (over a distance of up to $\sim 100\text{ }\mu\text{m}$) alone. The static friction force, F_S , was then extremely high - at least an order of magnitude greater than the applied normal load. At lighter loads, the friction traces were similar to those observed in air, although the mean frictional resistance was higher. It was not unusual, after a short period of sliding, for the surfaces to "weld" strongly together; relative motion then ceased and F_S continued to increase as above. Increases in F_S due to topographical variations (e.g. surface steps) were also observed. Phenomena of this nature could be distinguished from adhesive "seizure" situations, since,



unlike the latter, their frictional behaviour depends upon the direction of sliding. Nevertheless, substantial increases in F_S (> 5 times the normal load) resulting from surface irregularities alone were detected.

Diffused bulk impurities were then depleted by means of successive cycles of heating and ion bombardment. Although complete removal was not possible, examination by AES revealed a reduction of the principal impurities to approximately one-tenth of the original concentration.

The friction traces obtained under these conditions were rather similar to those described above, being characterised by stick-slip and adhesive welding. A typical normal loading (R - P) curve is shown in figure 5(b). Note that the intermediate rise in R is now no longer observed.

5. Discussion

The results presented in the preceding paragraphs show that substantial differences in adhesion and frictional behaviour can be effected by changes in environmental conditions, magnitude of the normal load etc. Although only a limited amount of information has been obtained at this stage it should be possible, with due consideration of adhesion, frictional and electrical contact resistance characteristics, to attempt an explanation of the results obtained. Returning first to the experiments involving nickel-nickel contacts, it is evident that the mechanical behaviour in air is dominated by electrically insulating surface layers i.e. we are dealing with a nickel oxide-nickel oxide interface rather than pure nickel surfaces. Nickel oxide is considerably harder than pure nickel though rather brittle. Since no changes in R were observed during normal loading, we conclude that the loads involved were too small to penetrate the oxide film. The same applies to tangential sliding. In the latter case, frictional forces were too small to detect when very light normal loads were used. This means that there was insignificant mutual adhesion or penetration of the surface; consequently resistance to sliding was very small.

We infer, from the results obtained at higher loads, that it is possible to form a very shallow indentation in the flat sample leading to "ploughing" resistance (observed stick phase). As this increases, the oxide junction cracks and breaks apart (corresponding to slip) and the friction returns to a low value. Fracture of the junction could lead to exposure of fresh metal at the tip which in turn would be rapidly oxidised. This process could be repeated many times with successive cycles of fracture and reoxidation of the tip surface. Our interpretation of corresponding experiments conducted in UHV may be based to a large extent on observations of contact resistance during normal loading or sliding. For example, initial suppression of adhesion after contact (applied load $\sim < 30 \mu N$, unstable R) and the correlation between low R values and adhesive contacts (load $- > 30 \mu N$) points to the presence of shallow contaminant layer. (Although the specimen surface was not analysed by AES, there is less reason to suppose that this behaviour was due to interfacial surface roughness in which case less consistent results would be expected). Having observed the effect of a shallow contaminating film on adhesion we might expect it to have a similarly strong influence on friction. In the present experiments, it is difficult to determine and separate, on the one hand, frictional resistance due to ploughing and on the other the resistance due to adhesion. Certainly, there are regions where clean or virtually clean metal-metal contact occurs, as evidenced by reductions in R to values less than a few hundred Ohms. However, these are not strongly adhering, suggesting that the contact area (of clean metal) is very small. At high loads it may be possible to strip the surface film whilst retaining good electrical contact at the interface. The combined effects of adhesion and ploughing under these conditions would probably lead to complete seizure and this was not observed in these tests. Nevertheless, there is evidence that more frequent break-through of the film occurs with increasing load.

Turning now to the results pertaining to tungsten-nickel boride contacts, the main, and somewhat unexpected, feature of discussion concerns the reduction in

adhesion after cleaning (ion bombardment) of a contaminated surface. There are at least two possible explanations for this behaviour: First, although clean metals tend to adhere strongly, the same may not be true of crystalline/amorphous interfaces. If these are essentially non-adhesive, the "pull-off" or separating force should be negligible and the resistance to sliding, at light loads, most likely will be dominated by topographical variations at the interface, such as submicroscopic undulations resulting from ion bombardment. Assuming the above hypothesis to be true, the adhesive behaviour on a contaminated surface must be due to some favourable bonding between the clean tungsten tip and, for example, oxidation products or absorbed gases. Such an argument is reinforced by field emission measurements which revealed transfer of material to the tip after separation. On the other hand, it could be argued that what we really observe is a surface roughness effect. However, as discussed before (nickel-nickel contacts) this would probably reveal itself as a statistical variation in the data e.g. in the adhesive behaviour and therefore seems to be a less likely explanation.

Finally, we shall examine the results obtained for tungsten-titanium oxide contacts. There are several effects to be considered here. Instabilities in electrical resistance during loading and unloading in laboratory atmosphere suggest that overlying contaminating layers are either shallow, allowing tunnelling conductance or are thicker but broken through, in which case a temporary clean contact may occur albeit over a minute region. However, no stable contacts with low R were observed under these conditions. This is probably because the vibrational energy in the apparatus is somewhat greater than that required to separate the (very weakly) adhering surfaces. A further contributory factor may be the roughness of the titania surface. There is little doubt that the latter is of overriding importance during sliding of opposing surfaces; in this case frictional resistance is provided by gradients and/or surface steps and adhesion plays a negligible role. The fact that reasonably reproducible friction traces were obtained during repeated traversals

over the same region suggests that gross plastic deformation does not occur. However, the relative position of the abrupt slip towards the end of the trace (figure 3) in consecutive traversals indicates that some smoothing of the highest "peaks" may be taking place.

For experiments in vacuum, the R - P characteristics for surfaces containing appreciable amounts of diffused bulk impurities were more difficult to explain, at least as regards the increase in R following the initial abrupt drop to low R after contact. One possible cause is an increase in concentration of lower conductivity material just beneath the surface which is broken through only at comparatively high loads. This layer, if it exists, appears also to prevent strong adhesion at intermediate loads during normal loading. Corresponding friction experiments showed that the resistance to tangential motion depended to a certain extent on the load (or alternatively, the point reached on the R - P curve) but that seizure could be observed at any load. This fact leads us to believe that some ploughing or delamination of the surface occurs during sliding which, in turn, leads to enhanced conditions for adhesion. A process along these lines would occur only on relatively flat regions and represents the highest frictional resistance recorded during sliding. Of course, in other areas, there remains a significant contribution from topographical surface features. However, in general, the resistance to sliding due to surface roughness was less than that due to adhesion.

6. Summary and Conclusions

Further development of the apparatus originally described by Pollock *et al* [4] has enabled us to measure frictional resistance to sliding, between a sharply pointed tip and a flat foil or crystal at loads less than 1 mg, as well as adhesion at the interface when the two surfaces are separated. Additional information was obtained by measurement of electrical resistance throughout contact, field emission microscopy of the tip both before and after contact, and Auger electron spectroscopy of the flat surface.

The experiments confirmed that, under very light loads, clean metal-metal pairs tend to adhere in UHV whilst no such effect is observed in the laboratory ambient. As a result, during tangential sliding, the frictional resistance of clean surfaces is significantly higher in UHV than in air.

In the case of a metal-ceramic interface (tungsten-titanium oxide) the same general conclusions apply. However, the mean frictional resistance in air was at least as high as that found for clean metal interfaces in UHV. This effect appears to be due to surface roughness. In UHV, the mean resistance to sliding is even higher, leading to seizure.

For a crystalline-amorphous interface (tungsten on nickel-boride) a different trend emerged. Here, adhesion during normal loading was observed only in experiments carried out prior to cleaning of the flat surface. Furthermore, the resistance to sliding of the tungsten tip was significantly higher on the as-received surface.

7. Summary Of Plans For Future Experiments

This part of the work has now reached the stage where we are in a position to use our quantitative measurements to distinguish between various alternative models as outlined above. For example, by measuring contact area as a function of normal and tangential force, we can test the formula of Savkoor and Briggs referred to earlier:

$$F = \{6\pi w r (3\pi w r + P)\}^{1/2}$$

and at the same time verify that the contact radius a is varying with load according to the predicted equation:

$$K a^3 / r = \{6\pi w K a^3 - 3\lambda K F^2 / 16\}^{1/2}$$

(where K and λ are elastic constants), whereupon it may be possible to ascribe a

particular physical model to each combination of materials under the experimental conditions imposed. Ceramic-metal and ceramic-ceramic combinations are probably the least studied and understood and these necessarily will be investigated further.

Of particular concern also is the efficacy of special coatings such as ion implanted layers and vapour deposited films, in improving wear. We have already established a reliable indentation technique whereby the plastic and elastic properties of very thin coatings can be meaningfully compared. However, such results are not always sufficient to explain the observed behaviour. Although hardening of the surface is likely to be a contributory factor it is hoped that adhesion and friction experiments will contribute further to our understanding of the tribological behaviour of hard coatings.

Thus although the aims as originally outlined have not all been achieved, the research is being continued here along the lines originally planned, with good prospects of a real breakthrough within the next two years.

PART II

CHARACTERIZATION OF SUB-MICRON SURFACE LAYERS BY INDENTATION

1. Introduction

Mechanical testing by indentation is a long-established method of materials characterisation [1] but it is only since the early 1970's that it has been possible to carry out mechanical tests in miniature in which plastic deformation is limited to the top one hundred nanometres or less of the specimen [2]. More recently, with the advent of special sub-micron coating techniques such as ion implantation, instruments capable of rapid surface mechanical analysis at the submicroscopic level have begun to be developed. These have evolved along the lines of the macroscopic indentation "hardness" test although there are some important differences which will become apparent later. At the macroscopic level, hardness is usually defined as the load divided by the surface (or projected) area of the residual impression, the dimensions of the impression being sufficiently large to be measured by optical microscopy. Although this is a simple method it is now realised that hardness itself is a somewhat complex entity reflecting a combination of properties rather than a single fundamental one. Nevertheless, the test provides a wide spectrum of information ranging from approximate yield stress values [3, 4] to fracture toughness data [5] and even identification of active slip systems [6].

The main limitation of the conventional hardness test is the minimum size of impression that can be measured sufficiently accurately by optical microscopy (10-15 μm). It is therefore of restricted use in surface and fine-scale analysis. Recently, more sensitive instruments have been described [7, 8, 9] where the authors claim to be able to measure hardness on a scale commensurate with the depth of ion-implanted layers and other thin protective films. In this respect we have made use of the instrument described by Pollock *et al* [10] which is capable of rapid data acquisition on surfaces exposed to the normal laboratory atmosphere.

The technique has the advantage that each test results in a continuous curve of indentation depth against load for both loading and unloading, and in consequence, gives information on elastic recovery as well as plastic deformation - and, as we shall see later, on visco-plastic behaviour (time-dependence).

2. Aims

The aims of this work followed from the current understanding, or lack of it, of indentation experiments on this scale. Our first objective was to establish the minimum thickness of film or surface layer that could be meaningfully characterized using the present technique. In other words, at what critical ratio of indentation depth to film thickness is the measurement affected by the underlying substrate or bulk material. We cannot assume that the relevant macroscopic results are applicable here, nor that the same critical ratio applies to different material combinations i.e. hard films on soft substrates and soft films on hard substrates. Further complications arise from surface effects (e.g. contamination) and scaling factors (influence of the size of the deformed volume).

Secondly, in conjunction with our colleagues in France, we intended to investigate the influence of ion implantation on the mechanical properties of metals. Specifically, we were concerned with (a) boron and phosphorus implantation into nickel (b) nitrogen implantation into titanium. Our priorities were to study the effects of radiation damage and hardening of surfaces implanted with ions at low, intermediate and high fluences (concentrations) and particularly any significant changes in properties resulting from the progressive amorphisation of the surface as the implanted dose increases; and also the beneficial effect (if any) of complete amorphisation of the surface and possible further changes following annealing and recrystallisation.

Our final objective was to gain a better understanding of time-dependent effects (indentation creep) at the submicrometer level as recently reviewed by

Pollock *et al* [10]. It is known that significant creep occurs in some metals, even at room temperature, in a constant load indentation test over a period of several hours. Here, however, our chief intention was to explore the phenomenon of low-temperature plasticity over a much shorter time-scale (less than one minute): since the apparatus is designed for very high depth sensitivity (rather than long-term stability with respect to thermal drift), it is well suited to this type of investigation.

3. Description of Apparatus

The equipment (shown in Figure 1) is based on earlier work [7] involving continuous recording of penetration depth as a function of load or of time. In the experiments described below, the load (between $10\ \mu\text{N}$ and $30\ \text{mN}$) was applied electromagnetically to a three-faced pyramidal diamond indenter, for which a 90° angle between edges was chosen. For such a "sharp" indenter, friction between it and the specimen is likely to be significant, but this disadvantage is often outweighed by an earlier finding [11] that for rougher surfaces, sharp indenters give more consistent results. The indentation depth was measured with a capacitor bridge arrangement which was recalibrated, whenever the initial indenter position was altered, with the help of a piezoelectrically controlled movement. Specimens could be transferred between two locations (test and microscopic position) using a rotatable turret. Particular areas of interest were identified in the microscope and then transferred to the test position or relocated by means of a computer-controlled three-axis (x, y, z) movement. The resolution of the depth measurement was estimated to be better than 1 nanometre, but both specimen roughness and vibration tended to limit the accuracy with which the moment of contact could be identified. In practice, the zero of plastic indentation depth could be determined with reasonable precision, as described below.

4. Interpretation of Data and Definition of Parameters

A typical experimental procedure is as follows. First, we obtain a preliminary

curve of indentation depth, δ , against time, t , the applied load, P , being held constant at a value approximately equal to the maximum load of interest. The δ value always increases rapidly during the first few seconds: if, thereafter, its rate of change, $\dot{\delta}$, remains higher than, say 0.3 nm s^{-1} , a quite different "indentation creep" procedure is essential, as described later. Otherwise, we next carry out several plots of δ_T as a function of increasing P on different points on the specimen surface, keeping the loading rate the same for each plot. A different maximum load P_m is used for each plot, so that we obtain a series of loading-unloading curves whose hysteresis area, W_p , corresponds to the plastic work performed on the specimen. In the simplest case of a specimen exhibiting fully plastic deformation with hardness H independent of depth, indented by a pyramid, a graph of $W_p^{2/3}$ against P_m would be linear.

Next, from the raw "on-load" data we wish to assess separately the contributions made by elastic and plastic deformation. There is a partial recovery in the depth of the indentation as the load is removed, as a result of the release of stored elastic strain energy (which can provoke fracture in brittle materials). Since there is no complete theory of elastoplastic indentation, we make the following simplifying assumptions: (1) that a rigid pyramid (geometrically equivalent to a cone of semiangle ψ) is indenting an isotropic solid under conditions in which, on loading, any elastic displacement of the hinterland does not significantly affect the value of mean pressure, p_m ; (2) that the specimen is fully work hardened, with a high enough ratio of Young's modulus, E , to flow stress, Y , that p_m (which equals H , the hardness) approaches a value of $3Y$ (full plasticity in a polycrystalline material). Under these conditions, we may still detect elastoplastic rather than ideal rigid-plastic behaviour. A direct means of assessing the relative contributions of the two components of deformation during indentation - irreversible and reversible - is through the measurement of elastic recovery in the depth of the indentation as the load is slowly reduced to zero (the recovery in the diameter is very much

less but with Knoop indentations may still be measured [12]).

We use the notation of Newey *et al* [7] to describe a typical depth/load cycle (figure 2). In principle, it is possible to define at least four types of "hardness" whose values may be derived from such curves, knowing the indenter geometry and the maximum load applied:

- (a) an on-load or unrecovered hardness, involving δ_T ,
- (b) an off-load or recovered hardness, involving $\delta_T - \delta_e$,
- (c) a refined value of off-load hardness (theoretically closer to p_m), involving $\delta_T - \delta'_e$, which allows for the fact that a small but significant recovery in the diameter begins at Point A, and
- (d) a hardness close to the value obtained by the classic optical measurement of the diagonal (this derivation takes account of pile-up).

The derivations are complex and the most useful semi-empirical definition of *elastic recovery parameter* is that based on the model of Loubet *et al* [13], which assumes that the elastic unloading corresponds to that of a blunt punch, whose constant area, πa^2 , was determined by the plastic flow during loading. This implies that the elastic recovery occurs primarily in the hinterland beyond the plastically deformed zone. In practice, there is some recovery in area as well as in depth, but this is allowed for if our recovery parameter is defined in terms of δ'_e rather than δ_e :

$$R = \delta'_e / \delta_p$$

where δ'_e is obtained by extrapolation of the linear part of the unloading curve, this linearity confirming the validity of the constant-area punch model. (In cases where the elastic recovery is very large, the departure from linearity can be significant. We then take the quality $2W_e/P_m$ where W_e is the released elastic work associated

with the unloading curve, as the best measure of δ'_e). We can express the physical significance of this parameter R as follows. The maximum load P_m determines δ'_e according to:

$$P_m = \pi a^2 H = \alpha \tan^2 \psi \delta_p^2 H$$

where ψ is the semi-angle of the equivalent indenter cone and α is the appropriate geometrical factor, with (following the blunt punch elastic unloading model) P_m being also equal to

$$= \frac{E}{1 - \nu^2} 2a\delta'_e$$

Thus, $\delta'_e = \pi a H (1 - \nu^2) / (2E)$ so that the simple ratio of δ'_e to δ_p defines the quantity R that is independent of load:

$$R \equiv \frac{\delta'_e}{\delta_p} = \frac{H}{E} \sqrt{\frac{\alpha \pi}{4}} (1 - \nu^2) \tan \psi$$

which gives a measure of $H \tan \psi / E$ as the basic parameter derived.

We are now able to "correct" the raw on-load data to give values of the off-load depth δ_p which characterises the *plastic deformation*. For a given specimen, all the loading curves are superimposed and averaged by computer. Knowing R at 6 to 10 different depths, we subtract the appropriate value of elastic depth recovery from the averaged δ_T curves to obtain δ_p as a function of P . Because of uncertainty in the zero of δ , where possible it is best to plot graphs with δ_p itself (rather than some function of δ) as the abscissa: in the simplest case of a specimen showing fully plastic behaviour with hardness, H , independent of δ , we would expect $P \propto \delta_p^2$. We normally plot δ_p against $P^{1/2}$ and, where necessary, $W_p^{2/3}$ against P_m . In the simplest case, both graphs are linear for at least part of the range of load, and extrapolation gives agreement as to the δ -zero at which

plastic deformation begins. To enable absolute values of hardness to be obtained, the indent area may be measured by electron microscopy [9] but if time does not permit the use of this delicate procedure, the gradients of the two types of curve allow one to derive values of two "plasticity indexes" (relative hardnesses)

$$I'_p \equiv \left(\frac{d\sqrt{P}}{d\delta_p} \right)^2;$$

and

$$I_H = \frac{d(P^3)}{d(W_P^2)}$$

or, in nondifferential form, $I_p \equiv P/\delta_p^2$; $I_H \equiv P^3/W^2$.

The indenters used being trigonal diamond pyramids of nominal angle 90° , the hardness H is nominally equal to I_p/k or $I_H/(9k)$, where $k = 2.6$, but because of possible small variations in geometry between indenters, we prefer to present the data in the form of I_p^* and I_H^* values; these are defined as values of the plasticity indices normalized with respect to the appropriate single constant value obtained on a reference specimen (silicon of known doping). Periodic tests are performed upon this silicon control, any indenter blunting or other change in test conditions thereby being immediately detected. Subject to the uncertainties arising from the existence of time-dependent behaviour and other approximations involved, one can regard a material for which I_p^* or I_H^* has the value unity, as having the same hardness as the silicon control.

5. The Thin Film or Bilayer Problem

It is well known that most indentation hardness measurements reflect a combination of elastic and plastic properties of materials and that the plastically deformed zone around a permanent impression extends well beyond the perimeter of the impression, up to 30 times its depth for single crystals [14] although considerably less for polycrystalline materials [15]. The elastic "envelope" presumably

extends to still greater depths but this is much more difficult to quantify. Since our first objective was to measure the intrinsic properties of thin films, we wished to know the critical ratio of indentation depth, δ , to film thickness, h , beyond which the measurements are affected significantly by the expansion of the elastic/plastic zone into the adjacent substrate.

As a first guide, the U.K. National Physical Laboratory [16] recommends that the indentation depth should not exceed one tenth of the thickness of the region of the specimen that is being tested. A more rigorous, theoretical approach has been attempted by Lebouvier *et al* [17]. Their analysis suggested that the critical ratio should depend upon the yield strengths of the film and substrate. Accordingly, we describe here the results of attempts to measure $\delta : h$ for soft microcrystalline nickel films on a hard silicon substrate and for hard films on soft substrates (niobium oxide on niobium and also nickel-boron on nickel). The aim was to establish the range of depths and minimum film thickness for which such measurements do, in practice, characterize the film material itself, seeing that the relevant macroscopic theory does not necessarily apply on such a small scale.

5.1 Experimental

5.1.1 Specimens

Soft films were prepared by vapour deposition of pure nickel to depths of 150, 300 and 600 nm respectively onto monocrystalline silicon slices. The grain size of the nickel coating was approximately 50 nm in each case.

Hard films on a soft substrate were of two types and comprised (i) amorphous niobium oxide of constant composition, prepared to different thicknesses by anodic oxidation of pure niobium, and (ii) homogeneous nickel-boron layers of uniform composition and constant thickness achieved by multi-energy ion implantation of boron into pure polycrystalline nickel (grain size ca. 100 nm). To produce different levels of lattice disorder (including complete amorphisation of the nickel), a range

of specimens of different boron concentration were prepared. (Further details of these specimens are given in [18]).

5.1.2 Results

Details of how values of the relevant material parameters are derived from the raw $\delta - P$ data have been described already. In the depth/load experiments here we attempted to minimise the indentation creep effects by choosing a suitable loading rate, normally 0.1 mN s^{-1} ; periodic checks were made in order to verify that variations within the range 0.05 to 0.15 mN s^{-1} had no major effect upon the value of depth at a given load.

5.1.2.1 Soft Films on a Hard Substrate

Figure 3 shows a series of loading and unloading curves obtained with a thin (150 nm) film of nickel on silicon. For the same film, and for the uncoated substrate, figure 4 shows $W_p^{2/3}$ as a function of P_m . The silicon plot is indeed reasonably linear, while the graph for the 150 nm thick film shows a change in gradient at a load of 2 to 3 mN, which as we shall see later, corresponds to a depth slightly greater than 200 nm. Elastic recovery parameters, R , were calculated for each specimen and plotted as a function of the plastic (off-load) depth as shown in figure 5. In theory, for a homogeneous specimen R should be inversely proportional to the ratio of Young's modulus to yield stress, and thus it is not surprising that as shown in figure 5, the thinner films have the higher values of R and show a shift in the value of R as the indentation depth is increased. For the two thinnest films, even at the smallest depths the effect of the substrate is felt. The off-load depth, δ_p has been plotted as a function of $P^{1/2}$ also. Referring to figure 6, we see that with bilayer specimens a decrease in slope is seen, corresponding to an increase in hardness, as with the $W_p^{2/3}/P_m$ graphs, and at the same load. For example, for the 150 nm thick film this change was seen at $\delta_p \approx 250$ to 230 nm. At higher loads the slopes of the $\delta/P^{1/2}$ curves for Si and for the 150-nm film

do not differ significantly; the two specimens have the same "differential" off-load hardness. However, to a very great depth the two curves remain separated and the effect of the nickel upon the apparent hardness itself persists.

Figure 7 shows values of I_p^* (already defined in previous section) as a function of δ_p/h , for three different film thicknesses. The substrate alone shows very little variation with depth, as expected from the linearity of the $W_p^{2/3}/P_m$ curve in figure 4. For the thinnest film, three sections of the curve may be distinguished. At shallow depths (less than ca. 30 to 50 nm, section O-A of the curve,) I_p^* decreases until a plateau (A-B) is reached. Without further evidence it is not possible to decide whether section O-A represents a significant change in material property near the surface or merely an artefact of the technique such as finite curvature of the indenter. For all nickel on silicon specimens, this plateau appears always at the same value of I_p^* , namely 0.37 ± 0.05 , which we therefore take as the intrinsic value for nickel in the form used here. Note that bulk nickel of grain size ca. 100 nm is found to be very much softer ($I_p^* = 0.07$). I_p^* then rises (section B-C) as expected, as the indenter approaches the substrate, this rise corresponding to the change in slope seen in figs. 4 and 6. The critical value of δ_p/h above which the substrate begins to be felt is ca. 1.5 for $h = 150$ nm (for the thicker films, this depth was not reached even at the maximum loads attainable; for $h = 300$ nm, $(\delta_p/h)_{crit} > 1.7$). However, the effect of the soft film is still felt at $\delta \gg h$, in that I_p^* for silicon has not been reached even at $\delta_p = 2h$. A practical point may be emphasised here. We often find that the presence of a very thin soft film can have surprisingly little effect upon δ_T , so that the depth of the film/substrate interface is hard to determine from the raw loading curves alone (without taking the values of W into account). This is because at a given load, in the presence of the soft film (case A), δ_p will be greater than when no film is present (case B). However, the load is spread over a larger area in case A, so that δ'_e is less than in case B. Thus the difference between the totals $\delta_p + \delta'_e = \delta_t$ is quite small and can be lost

in experimental scatter.

5.1.2.2 Hard Films on a Soft Substrate

Figure 8 shows results obtained for a film of niobium oxide (Nb_2O_5) of thickness 270 nm on niobium. Data obtained at small depths (section A-B, 50 to 200 nm) are reasonably consistent and confirm that the oxide is harder than unoxidised metal. At greater depths (point B), a "jump" in the curve is seen as the indenter penetrates abruptly into the underlying, much softer niobium, after which the I_p^* value is approximately equal to that of unoxidised niobium (section B-C). The $\delta/P^{1/2}$ curves A-B and B-C are reasonably consistent from one test to another, but the jump occurs apparently at random over a wide range of depths in the neighbourhood of the interface. For this type of specimen we were unable to investigate the effect of film thickness on $(\delta_p/h)_{crit}$, since for thinner films the jump into the underlying metal appeared to take place at the smallest values of δ at which consistent results were obtainable, so that $I_p^* = (I_p^*)_{\text{Nb}}$ always. We attribute this unstable behaviour to brittle failure within the bilayer, as occurs in the "indentation adhesion test" which Chiang *et al* [19] have used to measure fracture toughness of coating/substrate interfaces.

Effects of this kind are less likely in the case of Ni-B films prepared by implantation, where there is no abrupt interface or problem of adherence. Figure 9 shows $\delta/P^{1/2}$ curves for Ni and for Ni-25% B. The decrease in slope in the near-surface region O-A is less clearly evidenced than with the soft films (at low depths the elastic recovery and hence the uncertainty in δ_p were rather large). The section A-B of constant slope is assumed to characterize the Ni-B itself. The subsequent section B-C, of increasing slope, begins at a δ_p -value of 250 to 300 nm, approximately equal to the thickness of the implanted layer, as confirmed by the $W^{2/3}/P_m$ graph (fig.10), and even at the maximum depths attainable, the $\delta/P^{1/2}$ curves for Ni and Ni-B are still far apart. In figure 11 we have re-plotted the data in the form of I_p^* against δ_p/h . In contrast to the corresponding data for soft films

we see that the substrate has significant effect for δ_p/h greater than a critical value of ca. 0.8 ± 0.1 . The significance of the effect of boron concentration on hardness is discussed in later sections.

5.2 Discussion and Conclusions

A two-dimensional kinematic treatment of the fully plastic indentation of a bilayer in plane strain has recently been described [17]. It predicts that the mean indentation pressure should vary with the ratio w/h (where w is the half-width of the indentation) in two distinct ways, according to the ratio of the yield strengths Y_0 and Y_1 of film and substrate. If expressed in terms of δ_p/h instead of w/h , the detailed calculations may be broadly summarized by the prediction that when the film is softer than the substrate, the mean pressure will increase quite abruptly at a critical value of δ_p/h which varies within the approximate range 0.5 to 1.5 depending upon the value of Y_0/Y_1 . Our findings for nickel on silicon at this scale of indentation thus suggest that the influence of the hard substrate begins to be "felt" slightly later than expected (at δ_p/h values of the order of 1.5 to 2). When the film is harder than the substrate, the decrease in mean pressure with indentation depth is predicted to occur more gradually, the critical value of δ_p/h itself varying from ca. 0.4 for $Y_0/Y_1 = 1.5$, to 0.1 for $Y_0/Y_1 = 10$. From figure 11 we see that the Ni-B specimens are two to five times harder than the substrate, according to their composition; thus the observed critical value of δ_p/h (0.8 for Y_0/Y_1 greater than 4) is much greater than expected. Until such time as further work on indentation of bilayers on a macroscopic scale is reported, it is not possible to decide whether there is a real scale effect here, or whether it would be worth developing a model to include axisymmetric slip-line field solutions or one which took account of crystallographic texture or orientation of the film material. In any case, the results summarised in figure 11 show that a very thin hard surface layer can give an apparent hardness variation down to surprisingly large depths. Consequently, data suggesting, for example, surface effects such as a

depth-variation in an intrinsic property such as yield stress, should be interpreted with great care; it must be very hard to be sure of obtaining data that represent the material properties of underlying material, rather than those of an assembly of film plus substrate plus interface.

We conclude that it is difficult to estimate the intrinsic plasticity of the first 100 nm, particularly in the case of soft films: loading curves alone are not adequate. However, with additional data from unloading curves and measurement of plastic work, the method of continuous depth recording may be used to give a quantitative mechanical characterisation of the material, over a large range of depths within the layer. We propose that within this range, the plastic index I_p may be regarded as intrinsic to the film material (the value of the elastic parameter R , however, is determined by material properties over a much larger depth range). This conclusion applies to both the hard and soft layers that we have studied, except in the case of the unstable indentation behaviour shown by anodic niobium oxide films. For both hard and soft films, the effect of the substrate begins to be felt at an indentation depth/film thickness ratio significantly greater than predicted by macroscopic theory, and in the case of hard films, the effect can continue to a depth of more than two and a half times the film thickness.

6. Mechanical Properties of Ion-Implanted Surfaces

The technique of ion implantation as a means of improving the surface mechanical properties of materials is now well documented [20, 21]. As a general rule, ion energies are chosen so that only the topmost surface layers (first few hundred nanometres) are significantly affected. Mechanical characterisation must therefore be carried out on a similar scale (see previous section).

Recently, it has been recognised that, in some cases, the surface mechanical properties depend upon the fluence (concentration) of the implanted species. In this context, a particularly striking effect is partial or complete amorphisation of

the implanted layer at comparatively high ion doses. Although amorphous (glassy) films remain largely unexplored at the submicroscopic level, macroscopic tests on metallic glasses have shown that they are generally hard but less brittle than corresponding alloys and appear to have attractive tribological properties. For example, Takadoum *et al* [22] have observed that the seizure-resistance of nickel implanted with boron or phosphorus ions increased sharply when the metalloid content exceeded the amorphization threshold. Surfaces implanted with low B and P concentrations (in the range 0 to 10%) suffered severe adhesive wear. The friction coefficient and wear rate decreased abruptly when the amorphous fraction exceeded 50% (for about 15% B, P) whilst the surface topography became typical of a purely mild abrasive wear mechanism when the implanted layer was entirely amorphous (B or P concentrations exceeding 19%). In contrast, layers with compositions Ni_3B or Ni_3P , crystallized by annealing at 400°C or 600°C respectively, exhibited severe abrasive wear by crushing.

This raises the question of whether the increased wear-resistance was due to (i) an increased hardness, (ii) a higher ability to sustain localized deformation without work-hardening, (iii) an increased resistance to time-dependent effects which become noticeable even at room temperature for low strain rates at small depths, or (iv) the lower reactivity of amorphous films. The seizure-resistance of amorphous Ni-B and Ni-P films is certainly due, at least in part, to their lower reactivity compared with their crystalline counterparts, and this has recently been correlated with a difference in surface electronic structure [23]. However, the tendency to seizure depends also on the surface ductility and hardness, and the brittle behaviour of crystallised films during friction is solely due to a difference in the deformation mechanism.

In the experiments described below we have studied the influence of boron or phosphorus implantation into nickel and nitrogen implantation into titanium. Specimens of each of these were readily available to us through our colleagues

at Orsay, France. In the case of implanted nickel, we investigated the respective effects of radiation damage and solute hardening of surfaces, implanted with low boron or phosphorus concentrations, amorphous clusters formed at intermediate fluences, complete amorphization at high fluences, redistribution of defects in the glass after a relaxation anneal at intermediate temperature, and finally the effect of crystallisation by annealing at 600°C. These successive transformations were established previously on the basis of experiments using Rutherford backscattering spectroscopy. X-ray diffraction at grazing incidence and transmission electron microscopy [24, 25]. In addition, properties of amorphous nickel-boride produced by implantation were compared with those of single crystal trinickel boride (Ni_3B). For nitrogen-implanted titanium, the distribution of nitrogen atoms, defects and phases were correlated with changes in hardness depth profiles.

6.1 Boron and Phosphorus-Implanted Nickel

6.1.1 Specimens

Implanted specimens, prepared at Orsay, France, were received in the form of 1 mm thick foils measuring approximately 15 x 15 mm. Some were implanted in one stage with monokinetic ions of the same energy as for samples tested previously in friction [22] and giving comparable penetrations for B and P while others (B implants) were carried out in three stages in order to obtain a uniform concentration of B over a larger depth (250 nm). On each specimen the implanted area covered approximately 12 mm x 12 mm, the remainder being masked off during implantation so that comparative tests could be performed. Implantation parameters are given in table 1, where R_p is the mean projected range of the implanted ion, ΔR_p the straggling of the distribution and $C(R_p)$ the maximum of P or B concentration at the depth R_p . The purity and depth composition of implanted layers were analysed by glow discharge optical spectrometry (G.D.O.S.), secondary ion mass spectrometry (S.I.M.S.) and by R.B.S. Profiles for implantations at a single energy are discussed in detail elsewhere [26]. Films of composition close to Ni-25% B

were annealed for 30 min. in sealed tubes under vacuum at either 200°C or 600°C, in order to obtain respectively either relaxed or crystalline films of Ni₃B. Their purity after this thermal treatment was checked by G.D.O.S.: neither oxidation nor segregation of B or P was observed. In addition, two trinickel boride (Ni₃B) single crystals of (001) orientation were obtained. Of these, one was annealed at 400°C and then electropolished while the other had been bombarded with 90 keV B⁺ ions to a fluence of 3.5 x 10⁴ cm⁻². This gave a negligible increase in boron concentration (≤ 1%).

Electroless films of NiB and NiP (8 μm thick and deposited on an ion substrate containing 3.3%B, 14.2%B, 25.4%B and 17.4%P were used as bulk standards despite the fact they contain impurities (up to 2% Pb in the Ni-B film with highest B content) and that they exhibit a columnar structure, the columns being about 1 μm in diameter. Measurements of their plasticity at the submicron level could be compared to their macroscopic hardness measured in a Vickers test.

6.1.2 Results

Figures 12 and 13 show $\delta = f(P^{1/2})$ plots for pure Ni and surfaces implanted at a single energy with increasing fluences of boron or phosphorus. These show that the "on-load" (unrecovered) hardness increases with the implantation fluence. The maximum hardening (figure 14) is reached at a dose slightly higher than 10¹⁷ boron /cm², i.e. when the implanted layer is half amorphous at R_p , and higher does have little strengthening effect. However in the case of phosphorus implantation the hardening almost saturates for influences as low as 10¹⁶/cm², and this element strengthens the surface less efficiently than boron. It is interesting to note that the seizure-resistance of Ni-P amorphous films implanted at the same energy is higher than for Ni-b [22, 23].

Figures 15 and 16 show some of the $\delta_p = f(P^{1/2})$ and $\delta'_e = f(P)$ curves for homogeneous Ni-b films implanted at three energies. Although we do not have

tribological data for these specimens for comparison, the values of I_p here (figure 17) are more significant than in the case of specimens implanted at a single energy (figure 14), since the slopes of the δ_p plots remain constant over a larger range of depth about 250 nm: the data on depth-dependence were presented in section 5.1.2.2. For this reason I_p and R -values measured for the thickest implanted films are the highest, and are comparable with those of bulk electroless deposits; I_p can be considered to represent an intrinsic property of the film, as has been discussed earlier.

Both plasticity index and elastic recovery parameter increases steeply for B or P concentrations in the range 0 to 2.3%, corresponding to the stage of swelling of the Ni lattice due to the insertion of B or P atoms and of formation of numerous dislocations during implantation [24, 25, 27]. We note from the I_p values that a Ni-3%B electroless deposit (a super saturated solid solution of B in a f.c.c. Ni matrix [28] is as hard as a highly damaged implanted film of similar composition. At higher concentrations, a striking difference appears between the effects of the two implants. As we see from figure 14, the hardening effect produced by phosphorus depends just upon this disordering or damage: thus a disordered but crystalline film (implantation of 10^{16} P/cm²) is almost as hard as partially or completely amorphous films. In contrast, the hardening effect of boron (figures 14 and 17) is correlated with the fraction of amorphous material present. Thus, for the range of concentrations (3 to 19% B) at which amorphous clusters form and multiply while the disorder in the residual crystal levels off [27], the parameters increase more gradually (table 2). The plasticity index remains constant for completely amorphous films of increasing boron concentrations in the range 19 to 40% and appears to be independent of the method of preparation; that is, whether prepared as amorphized Ni₃B on the underlying single crystal or in the form of amorphous Bi-25% on underlying soft nickel (see figure 18) moreover at small depths, the elastic recovery parameter is comparable for these two samples (figure 19). I_p

is greatest after a relaxation annealing inducing a densification of the glass and decreases slightly after crystallisation. It is interesting to note that although the latter is greater than the value obtained for amorphous Ni-25%B and amorphized trinickel boride, it is appreciably less than I_p for single crystal trinickel boride. This is opposite to the typical behaviour of a pure, cubic close-packed metal. However, this result is not unexpected if the chief role of the grain boundaries in this type of solid is to act as dislocation sources and thus to weaken the material, or possibly to induce cracking [29] as suggested by the unstable indentation behaviour referred to earlier. Table 2 lists the values of I_p relative to the value of 7.3 ± 0.5 GPa obtained for pure nickel (here we have not included values for the single-energy implants of non-uniform concentration, where I_p does not correspond to an intrinsic material property). For comparison we also give values of Vickers hardness relative to pure nickel, some from the literature and some measured by us. The most direct comparison possible is with the electroless deposits, where the agreement is to within 40 to 50%, the normalised H-values being consistently lower. However, the latter were not necessarily intrinsic to the film material, having been measured on deposits only 8 μm thick, and we note that the higher value reported for a metglass of comparable composition (Ni-15% to 20%B) is closer to the corresponding I_p -value.

Table 2 includes also values of I_p/R , and some macroscopic data on $E/(1 - \nu^2)$ for bulk materials of similar composition. For all alloys I_p/R is higher than for pure nickel. Contrary to expectation we have not found that the highest values are given by the crystallised films, which show brittle behaviour during friction.¹ R is determined by material properties over a larger depth range than I_p [10], and we cannot be sure that under the conditions of our experiments it represents an intrinsic property of the implanted layer. Nevertheless the ratio I_p/R

¹This poor tribological behaviour may more usefully be correlated with a different effect which we noted when indenting the crystallised films: sometimes, a "jump" in the δ/P curve was seen as the indenter penetrated into the underlying material. This unstable behaviour was also seen for Nb₂O₅ films on Nb and was attributed to brittle failure within the bilayer [18]

reaches a constant value below a certain depth, and agrees well, for a given Ni-B composition, between implant and deposit. It is greater for the supersaturated Ni-2.5/3%B solution than for the amorphous Ni-25%B, by a factor of 1.3 to 1.4, as would be expected [30, 31, 32]. We do not see a universal correlation between $E/(1 - \nu^2)$ and I_p , as should be found for a homogeneous material, but it may be noted that the irregular geometry of metglas ribbons introduces uncertainty in the reported macroscopic data [32] and that these values are normally measured under conditions of unidirectional rather than combined stresses.

6.1.3 Conclusions [52]

- (i) The introduction of boron or phosphorus into the nickel lattice, whether by ion implantation into the topmost surface layer or by bulk co-deposition in electroless films, produces a hardening effect. We have clarified how this depends upon atomic species and concentration, lattice disorder, and amorphous fraction.
- (ii) For both B and P, the lattice disorder produced by concentrations as low as 1.5% is enough to increase the plasticity index by a factor of more than 30%.
- (iii) At intermediate fluences, B appears to strengthen the surface more effectively than P. In the case of B, but not P, further hardening at higher fluences is correlated with the change in structure (increase in amorphous fraction), especially as indicated by the on-load data for single-energy implants. This correlates also with the improvement in resistance to seizure, abrasion, erosion-cavitation or initiation of fatigue cracks given by boron implantation [22].
- (iv) A fixed, one-to-one relationship cannot be established between the amorphous or crystalline nature of the surfaces and their mechanical properties, since disordered crystalline surfaces can be as hard as amorphous ones; the chemical nature of the addition must also be considered. In particular, the seizure-resistance of amorphous Ni-P surfaces must be attributed mainly to their low reactivity, since in this case amorphisation does not give any further surface strengthening beyond

that produced by lattice disorder. We are investigating the corresponding changes in surface thermodynamic properties by means of the UHV mechanical microprobe described earlier.

(v) For the amorphous compound prepared by either of two different methods (high fluence implantation of boron ions into pure nickel or low fluence boron ions into trinickel boride) good agreement was found in both plasticity index and elastic recovery parameters at small depths. The plasticity index for amorphous nickel boride is six times higher than for pure nickel but a factor of two lower than single crystal trinickel boride. The hardening correlates with the improvement in resistance to seizure, abrasion, erosion-cavitation or initiation of fatigue cracks given by boron implantation [22]. However, hardening alone is not adequate: the polycrystalline Ni-25%B, though softer than the single crystal when indented to depths of a few tens of nanometres, is significantly harder than the amorphous material and yet tends to suffer severe abrasive wear [22].

(vi) The additional hardening in Ni-B after a relaxation or crystallisation anneal seems to be consistent with existing hypotheses regarding the deformation mechanisms of glasses and their expected tribological performances [22]. Crystallized films occasionally showed a characteristic unstable feature in the indentation curve, possibly associated with their more brittle nature.

6.2 Nitrogen-Implanted Titanium

Compared with steels there are certainly fewer published data on the tribological properties of ion-implanted titanium or its alloys, but a certain amount of work has been devoted to the study of the influence of nitrogen implantation [33, 34, 35]. A summary of these results will be found in a recent article [36] which describes also a recent detailed compositional and chemical analysis of thin TiN films obtained by ion implantation. The same films, described below, were subjected to indentation tests in order to investigate their plastic and elastic behaviour.

6.2.1 Specimens

Samples of pure titanium, cut from rod, were implanted with $^{14}\text{N}^+$ ions in the Orsay machine. Implantations were carried out in three stages using successively smaller energies (see Table 3) in order to obtain an homogenous N concentration profile in the implanted layer over a depth of 500 nm. The nitrogen concentration (together with that for oxygen, carbon and titanium) in each specimen is shown in Table 3). Full details of theoretical distributions of implanted ions together with concentration measurements and depth profiles are given elsewhere [36].

6.2.2 Results

Figure 20 shows some of the raw curves for the film implanted with 50% N , and figures 21 and 22 the variation of δ_e , δ_p and $W^{2/3}$ with P , for the two highest concentrations and for pure Ti. As for other hard implanted films on a soft substrate previously studied with this technique [18], the elastic recovery exceeds that of Ti even at loads for which the substrate is penetrated : R is effectively constant ($25 \pm 1\%$) until $\delta_p = 500$ nm for 34 and 50% N instead of 5% for pure Ti (thus I_p/R and hence I_p will vary as I_p over the whole implanted thickness). On the other hand the curves $\delta_p = f(P)^{1/2}$ and $W^{2/3} = f(P)$ exhibit a change of slope for a load of about 7.3 mN, corresponding to a real penetration of implanted layers, δ_p of 350 ± 20 nm c.a. 0.7 times the film thickness. Note that a factor of 0.8 was also found in the case of Ni-B implanted films onto Ni with comparable hardness of films and substrate [18]. A faint shoulder is also observed in the $W^{2/3}$ curve of the Ti-50% N film at a load near 5.6 mN ($\delta_p = \text{ca. } 240\text{nm}$), which reflects that of the raw loading curves. For all the films studied, and even for pure Ti, a change of slope is also observed on the $W^{2/3}$ and δ_p curves at a critical load which depends on the film hardness: 2.5 mN for Ti and 1.25 mN for Ti - 34% N or Ti - 50% N . It is certainly due in part to the work hardening by polishing before indentation (especially for pure Ti and low N contents), and in part to the contribution of the unavoidable contamination film to measurements

at shallow depths. In the case of the hardest films (for which radiation damage and nitride hardening dominates over work hardening) this change of slope occurs at depths lower than 70 nm, as for hard NiB films: this seems to be the minimum film thickness for which the intrinsic hardness can be measured with our technique.

Note also that the plasticity index P/δ_p^2 and P^3/W^2 measured on the part of the curves intrinsic to the TiN films are always in the ratio (9 ± 0.5) , which fact helps to confirm the validity of the results. In order to analyse the influence of the N implantation upon the matrix hardness independently of the work hardening, the plasticity index, $I_p = P/\delta_p^2$, was normalized to the pure Ti value at each depth. The corresponding increase in off-load hardness is plotted as a function of the real penetration in the implanted film, δ_p , in figure 23. The agreement between the variations of hardness as a function of depth and N nominal content, and the variations of N concentration profiles or phase concentration profiles is very good as discussed in [36] (despite the change in thickness of contamination films, the apparent hardening at depths lower than 70 nm for all the films studied is perhaps due to the finite radius of curvature of the diamond tip, and thus is corrected by our normalization).

6.2.3 Discussion

Let us first compare the absolute hardness of pure Ti, measured by means of a Vickers test with indentation depths between 1 and 10 μm (well over the work-hardened thickness), with that of implanted films and of a TiN PVD coating studied, as deduced from their plasticity index normalized to Ti. The hardness of Ti being 2.5 ± 0.1 GPa (Vickers) and its plasticity index 20 ± 1 GPa (at large depths where it is not work hardened), the Vickers hardness of the outer layer of δ -TiN formed on the Ti - 50% N and Ti - 34% N implantation films would be 17.5 ± 1.5 GPa (as deduced from I.p). Similarly, for the δ -TiN PVD coating, a constant hardness of 52.5 ± 2.5 GPa was calculated for indentation depths of between 25 and 200 nm; and a value of 40 ± 5 GPa was obtained for indentation depths of

between 300 and 1000 nm by means of a Vickers test (this is a crude estimation because Vickers hardness tests were performed on thicknesses for which the result must be considered with caution, since the coating was only $5.7\text{ }\mu\text{m}$ thick. Taking this into account, the two values are in good agreement, but very much higher than reported values of the hardness of bulk TiN (17 to 23 GPa according to the author) [9, 10, 37] or those of various CVD coatings of δ -TiN or ϵ -Ti₂N (ranging between 12 and 27 GPa) [38]; but often the latter type of measurement is made by means of a Vickers test on thicknesses for which the substrate alters the result, and a wide range of structures and crystallographic textures is involved. The PVD coating studied here had a columnar structure with a diameter of columns of about $1\text{ }\mu\text{m}$ and a marked fiber texture. On the contrary, implanted films are formed of submicroscopic grains with isotropic orientations. These preliminary remarks illustrate the relativity of the concept of hardness, which depends on the scale at which it is measured with respect to the size of mobile defects. Values of the Young modulus were also derived from H/R , equal to 110 GPa for Ti-50% N film and 490 GPa for the δ -TiN coating; in the two first cases these values are very close to those measured by tensile tests, namely 120 for Ti and 78 to 84 for TiN [37].

Now as the concentration is varied, the changes in the depth profile of hardness and in its maximum value account for the expected effects of the creation of damage (2% N), hardening by solute N atoms in α -Ti (10% N), formation (20% N) then expansion (26% N) of Ti₂N, and finally formation (34% N) then expansion (50%) of TiN. Indeed the hardness exhibits alternately a maximum at a depth near 100 nm (for 2%, 20%, 34% N) or near the surface (for 10%, 26% 50% N), corresponding to the distributions of N and of the nitride phases in the first 200-300 nm of the surface [36]. The hardness levels off at depths of between 200 and 400 nm corresponding to a more oblate peak of the N sum-profile (at a depth near 290 nm for 2%, 10% N) or of the deeper elemental profile (at a depth near 400 nm for

20% to 50% N) [36]; the phases observed at these depths are also a mixture for Ti-34%N and Ti-50%N in the same range of depths, where inverse gradients of the δ -TiN and ϵ -Ti₂N concentrations were revealed by X-ray diffraction experiments, is close to the hardness of the pure Ti₂N film formed for lower N concentrations.

7. Time-Dependent Effects at the Submicrometre Level

We have seen that often there is a simple relation between indentation depth δ and load P ; for example $\delta \propto P^{1/2}$ for fully plastic deformation with uniform hardness. However, when δ varies significantly with time as well as load, then even if the rate of loading is kept constant, such simple relations will no longer apply. Accordingly, we shall first discuss time-dependent plasticity at constant load. Measurement of "indentation creep" parameters forms an important part of the characterization of the subsurface region of a specimen. It is also useful [39, 40] to study the relationship between indentation creep and scratch hardness. The fundamentals of indentation creep have recently been summarized in Maugis's review [41] of creep, hot hardness, and sintering in the adhesion of metals at high temperature. Recently Hooper and Brookes [42] have detected an "incubation period" in lead at high homologous temperatures (≈ 0.5), at which thermal recovery offsets work hardening [40]; Naylor and Page [43] have listed relevant deformation mechanisms in ceramics. Here we shall be concerned primarily with indentation creep in metals below about $0.2 T_m$, where T_m is the melting point on the absolute scale. Several examples [44,45] are known of cases in which indentation creep is more significant at submicrometre depths than in macroscopic tests at the same temperature. The continuous depth recording techniques used for loads below 10 mN prove to be well suited to the investigation of indentation creep.

In a constant-load indentation creep test, the stress, of course, decreases with time (unless a flat-ended punch [46] is used). Gerk [45] was able to calculate the time-dependent hardness in a case in which the relationship between dislocation velocity and stress was known. In general, however, it is important to find the

appropriate relationship between the strain rate and the measured rate of increase of the diameter or depth of the plastic indentation: in a hardness test, what is the effective strain? Tabor [47] showed empirically that indentation by a Vickers pyramid of metals that are not fully work hardened appears to produce a strain of around 8%: this is in addition to any pre-existing strain and applies to the situation at large t that is, after all the plastic deformation and associated work hardening has taken place. If the load and the indentation depth are then increased, the strain, ϵ , remains constant at around 8%: yet the plastic flow rate may well be significant, in which case $\dot{\epsilon} > 0$! An answer to this paradox was implied by Atkins *et al* [48], who argued on the basis of a model involving an expanding hemispherical cavity that at a distance, r , from the center of the indentation, the strain rate is given by

$$\dot{\epsilon}_r = k_2 a^2 \frac{\dot{a}}{r^3} \quad (1)$$

where a is the radius of the indentation and k_2 is a geometrical constant of value $3/2$ [47]. Using a plasticity equilibrium condition that gave the maximum stress, σ_m , as a function of $(\partial\sigma/\partial r_{t,a})$, and a theoretical creep expression for $\dot{\epsilon}$ as a function of σ_m and t , they thus obtained a differential equation for the stress, σ , which they were able to integrate over the whole volume (at constant t and \dot{a}) in order to obtain the hardness, equal σ_m , as a function of t . We may note in particular three aspects of the AST analysis:

1. It is not necessary to derive an expression for ϵ itself, for example, as a function of the size of the indentation;
2. $\dot{\epsilon}$ is associated with the rate at which the plastic/elastic boundary moves on into the material;
3. The procedure becomes very complex if no analytical solution to the differential equation for σ exists (this is the case for many creep expressions). However,

if we can measure $\dot{\epsilon}_r$, directly with the help of Equation 1, then the rest of the AST procedure is not necessary; we may test any theoretical plastic flow expression directly, without having to calculate the time-dependence of the hardness itself. Following this simple idea, we made the approximation that the strain rate $\dot{\epsilon}$, as predicted by any *physical* model for creep, may be identified with the value of $\dot{\epsilon}_r$, in Equation 1, at $r = a$, where it has its maximum value. For a fully plastic conical indentation, the depth, δ , is proportional to a , so that we have

$$\dot{\epsilon} \simeq k_2 \frac{\dot{\delta}}{\delta} \quad (2)$$

We may use our technique of using continuous-depth recording to measure $\dot{\delta}$ as a function of t at constant load (decreasing stress, σ) in a single test, without the need for a series of indentations with different loading times. We thereby observe directly how $\dot{\epsilon}$ varies with decreasing σ . (It should be noted that several approximations are involved: detailed effects of indenter shape, the nonhomogeneity of stresses and strains, and the elastic properties of the hinterland are neglected, and this approach will certainly not be valid in all situation. Matthews [49] has shown that for time-dependent indentation by a sphere, involving progressive work hardening, the AST spherical cavity model is inappropriate and a more complex argument should be used, involving differential and integral operators acting on the stress and strain according to the properties of the appropriate rheological model. We do not claim that the model described here is sufficient to explain indentation creep curves from start to finish. However, it does appear to be the simplest model with which the measurements can usefully be compared).

Regarding plastic flow mechanisms for predicting $\dot{\epsilon}(\sigma, t, T...)$, the literature makes use of the alternative "constant structure" and "steady-state structure" formulations, which refer to microstructural state variables such as dislocation density [50]. These variables may, for example, be fixed, or may be uniquely determined by σ and T ; in either case we refer to "steady creep". On the other

hand, for various reasons (such as work hardening), it may be necessary to include t , as an explicit variable, within the expressions describing the state variables and $\dot{\epsilon}$: here we have "transient creep" $\dot{\epsilon} = f(\sigma, T, t)$. Indentation creep below $0.25 T_m$ has generally been difficult to detect; here, at the stress values used, deformation mechanism maps [50] predict that we should observe low-temperature plasticity rather than creep (note that, strictly speaking, the term *creep* is used only when $\dot{\epsilon}$ varies relatively slowly with σ , the dependence being typically power-law; in low-temperature plasticity, the dependence is exponential. However, for simplicity we use the term *indentation creep* throughout).

We next examine the consequences of the simplest low-temperature creep model, based on a dislocation glide mechanism in which the dislocation velocity is limited by weak obstacles (activation energy barrier $\leq 0.2 \times \mu b^3$, where μ is the shear modulus and b the Burgers vector). Following Frost and Ashby [50], the strain rate is then given by

$$\dot{\epsilon} = \nu_0 \exp\left\{-\frac{\Delta F}{kT} \left(1 - \frac{\sigma}{p_0}\right)\right\} \quad (3)$$

where ν_0 is a frequency ($\approx 10^6 \text{ s}^{-1}$), ΔF is the activation energy characterizing the strength of a single obstacle, k is Boltzmann's constant, and p_0 is the athermal yield pressure. Replacing $\dot{\epsilon}$ by $k_2 \dot{\delta}/\delta$ (Eq. 2), and defining a *characteristic time*, t_c , and a *characteristic distance*, δ_c by

$$t_c \equiv \frac{k_2}{\nu_0} \exp \frac{\Delta F}{kT} \quad \delta_c \equiv \left(\frac{2\Delta F P}{kT k_1 p_0} \right)^{1/2} \quad (4)$$

we obtain

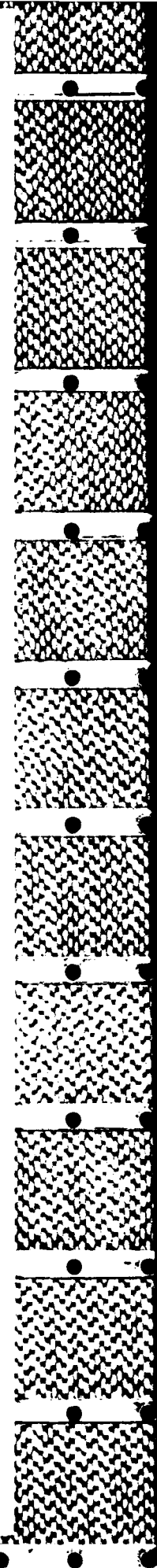
$$\ln \frac{\dot{\delta}}{\delta} = -\ln t_c + \frac{\delta_c^2}{2\delta^2} \quad (5)$$

where k_1 is the geometrical constant relating δ^2 with the projected area of indent

if we assume fully plastic deformation by a pyramidal indenter [$\sigma = P/(k_1\delta^2)$]. Thus, using the technique of continuous depth recording, from direct observation of δ and $\dot{\delta}$ at a known constant load, we may determine δ_c and hence the basic creep parameters ΔF and p_0 ($k_1 p_0$ may be regarded as an "athermal yield index").

In this elementary form, the model thus leads to two predictions: first, whatever the load, a time $t \gg t_c$ and a depth $\delta \gg \delta_c$ will, at length, be reached at which the stress term in Eq. 3 becomes negligible, $\dot{\epsilon}$ becomes constant, and δ increases exponentially with t . This surprising result is somewhat unlikely to be seen in practice, however, owing to work hardening at great depths and the inaccuracy of Eq. 2. A more important prediction is that if we wish to define the hardness at a given load or depth, it is best to restrict the conditions of the corresponding hardness test so that $0.1 t_c \leq t \leq t_c$. Within this region the hardness will show the least amount of variation with loading time [at $\delta = \delta_c$ its value, $P/(k_1\delta_c^2)$, will be $1/2kTp_0/\Delta F$]. Further complications arise if we wish to investigate how the hardness varies with load or to interpret the results of microindentation tests in which δ is measured as a continuous function of P . Even if the material properties are independent of depth, the expected $\delta \propto \sqrt{P}$ relation will not be obtained if creep is significant. Furthermore, unless the indentation depth can be expressed in terms of separable functions of stress and time, the hardness, even if defined for a particular (constant) value of loading time, will not be independent of load. These conclusions will be valid also in cases where, for example, a constant-viscosity or other creep model applies.

Figure 24(a) shows the result of a typical creep test at constant load: the specimen was a polymer (polyethylene terephthalate), and consequently time-dependent effects are very evident. In this case, viscous behaviour is seen, in that the graph of $\dot{\delta}/\delta$ against P/δ^2 (figure 24(b)) is approximately linear over a wide range. The more delicate experiments needed to explore time-dependent behaviour in metals are still in progress. When these are complete, we should be



able to predict the conditions under which a full characterisation should include a determination of the values of the relevant creep parameters - as compared with the different conditions under which a measurement of hardness alone is adequate.

8. Future Objectives

There are an increasing number of examples of thin metallurgical coatings being used industrially for reducing wear and improving reliability and lifetime of tools and machine components. In many cases the coating thickness is such that the microindentation technique described here provides one of the few possible ways of obtaining quantitative data on the mechanical properties of the coating itself, and could be increasingly useful especially if the results are correlated with data from scratch testing and adhesion experiments. At present, the range of materials of interest to us includes TiN, TiN_xO_y , Al_2O_3 and ion-assisted coatings of nitrides (or carbonitrides) of Ti, B, or Cr.

LITERATURE CITED

Preface

1. N.E.W. Hartley, *Thin Solid Films*, **64**, 177, (1979).
2. M.F. Ashby, K.E. Easterline, *Acta Met*, **32**, 1935, (1984).

Part I

1. D.H. Buckley, "Surface Effects in Adhesion, Friction, Wear and Lubrication", Elsevier, (1981).
2. H.M. Pollock, P. Shufflebottom, J. Skinner, *J. Phys. D.: Appl. Phys.* **10** 127, (1977).
3. N. Gane, P.F. Pfaelzer, D. Tabor, *Proc. Roy. Soc.*, **A340**, 495, (1974).
4. H.M. Pollock, *Vacuum*, **31**, 609, (1981).
5. H.M. Pollock, *J. Phys. D : Appl. Phys.*, **11**, 39, (1978).
6. S.K. Roy Chowdhury, N.E.W. Hartley, H.M. Pollock, M.A. Wilkins, *J. Phys. D : Appl. Phys.*, **13**, 1761 (1980).
7. H.M. Pollock, S.K. Roy Chowdhury, in "Microscopic Aspects of Adhesion and Lubrication", Ed. J.M. Georges, Elsevier, (1982).
8. M.D. Pashley, D. Tabor, *Vacuum*, **31**, 619, (1981).
9. S.V. Pepper, *J. Appl. Phys.*, **47**, 801, (1976).
10. S.V. Pepper, *J. Appl. Phys.*, **50**, 8062, (1979).
11. D. Maugis in "Microscopic Aspects of Adhesion and Lubrication", Ed. J.M. Georges, Elsevier (1982).
12. P. Heilmann, D.A. Rigney, *Wear*, **72**, 195, (1981).
13. K. Kendall in "Special Ceramics 8", (Inst. Ceramics) in Press (1986).

14. A.R. Savkoor, G.A.D. Briggs, Proc. Roy. Soc., **A356**, 103, (1977).
15. U. Marx, H.G. Feller, Metall., **33** 380 (1979).
16. M. Barquins, Materials Sci and Eng., **73**, 45, (1985).
17. J. Skinner, N. Gane, J. Phys. D : Appl. Phys., **5**, 2087, (1972).
18. L.B. Wilner, IEEE Trans. Ind. Electron. Control Inst., **16**, 40 (1969).
19. P.T. Squire, J. Phys. E : Sci. Inst., **12** 22, (1979).

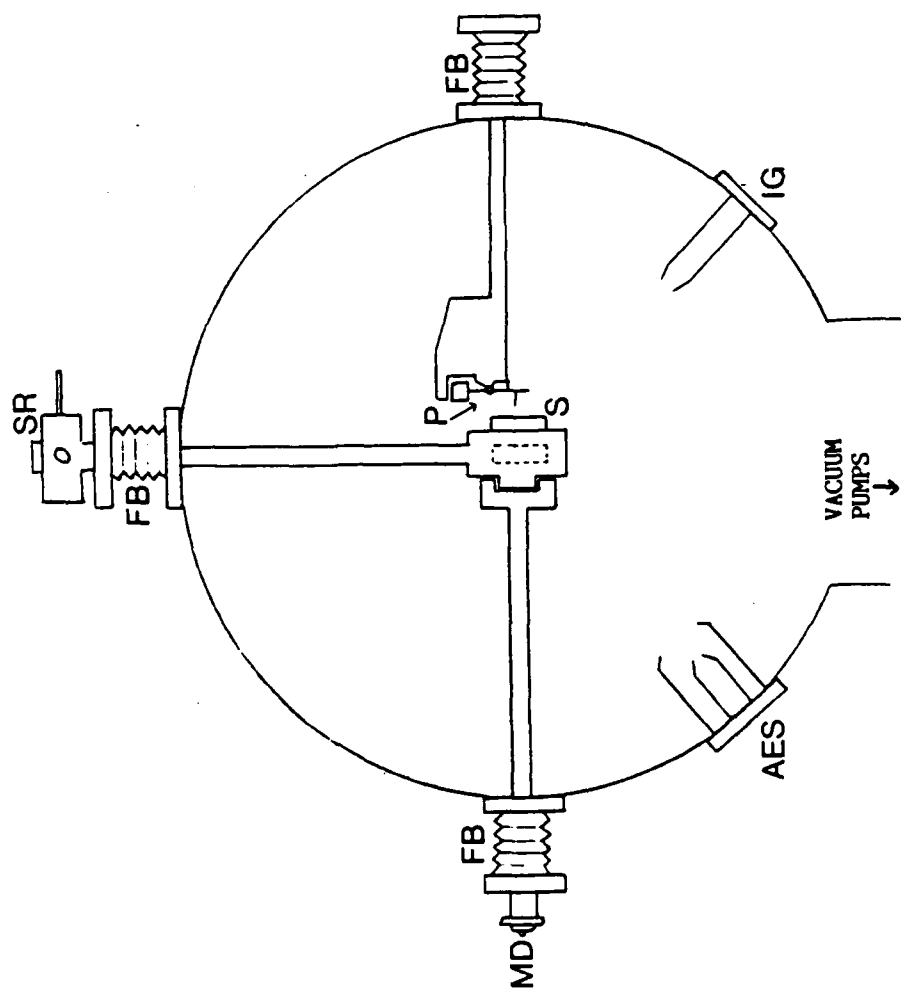
Part II

1. D. Tabor, Rev. Phys. Tech., **1**, 145, (1970).
2. N. Gane, Proc. Roy. Soc., **A317**, 367, (1970).
3. R.M. Douthwaite, J. Iron and Steel Inst., **208**, 265, (1970).
4. J.N. Robinson, A.H. Shabaik, Met. Trans., **4**, 2091, (1973).
5. A.G. Evans, E.A. Charles, J. Am. Ceram. Soc. **59**, 371, (1976).
6. C.A. Brookes, R.M. Hooper, W.A. Lambert, Phil. Mag., **A47**, L9, (1983).
7. D. Newey, M.A. Wilkins, H.M. Pollock, J. Phys. E : Sci. Inst., **15**, 119, (1982).
8. M. Nishibori, K. Kinosita, Thin Solid Films, **48**, 325, (1978).
9. J.B. Pethica, R. Hutchings, W.C. Oliver, Phil. Mag., **A48**, 593, (1983).
10. H.M. Pollock, D. Maugis, M. Barquins in "Microindentation Techniques in Materials Science and Engineering" p.47, ASTM Special Tech. Publ. no.889, P.J. Blau and B.R. Lawn,eds. (1985).
11. D. Newey, H.M. Pollock, M.A. Wilkins, in "Ion implantation into Metals" p.157, Eds. V. Ashworth, W.A. Grant, R.P. Procter, Pergamon, Oxford,

- (1982).
12. P.J. Blau, *Metallography*, **16**, 1, (1983).
 13. J.L. Loubet, J.M. Georges, O. Marchesini, G. Meille, *Trans. Am. Soc. Mech. Eng. J. of Tribology*, **16**, 1 (1983).
 14. R.P. Burnand, Ph.D. Thesis, University of Exeter, 1974.
 15. J.D.J. Ross, Ph.D. Thesis, University of Exeter, 1985.
 16. G.N. Peggs, I.C. Leigh, Report No. MOM62, U.K. Nat. Phys. Lab., (1983).
 17. D. Lebouvier, P. Gilormini, E. Felder, *J. Phys. D. : Appl. Phys.*, **18**, 199, (1985).
 18. J.D.J. Ross, J.C. Pivin, H.M. Pollock, J. Takadoum, To be published in *Thin Solid Films* **148**, 171 (1987).
 19. S.S. Chiang, D.B. Marshall, A.G. Evans in "Surfaces and Interfaces in Ceramic and Ceramic-Metal Systems", p.603, Eds. J. Pask, A. Evans, Plenum, (1981).
 20. I.L. Singer, *Mat. Res. Soc. Symp. Proc.*, **27**, 585, (1984).
 21. H. Herman, *Nucl. Inst. Methods*, **182-183**, 887. (1981).
 22. J. Takadoum, J.C. Pivin, J. Chaumont, C. Roques-Carmes, *J. Mat. Sci*, **20**, 1480, (1985).
 23. J.C. Pivin, J. Perreau, C. Reynaud, J. Takadoum, Accepted for publication in *J. Non-Crystalline Solids*.
 24. M. Schack, Thesis No. 667, Universite de Paris-Sud, Orsay, France.
 25. C. Cohen, A. Benyagoub, H. Bernas, J. Chaumont, L. Thome, M. Berti, A.V. Drigo, *Phys. Rev.*, **B31**, 5, (1985).

26. J. Takadoum, J.C. Pivin, J. Pons-Corbeau, J. Berneron, J. Charbonnier, *J. Surf. Interface Analysis*, **6**, 174, (1984).
27. R. Moreton, J.K. Lancaster, *J. Mat. Sci. Letters*, **4**, 133, (1985).
28. K.H. Gorbunova, H.V. Ivanov, V.P. Moiseev, *J. Electrochem. Soc.*, **20**, 613, (1973).
29. P.M. Sargent, T.F. Page, *Proc. Brit. Ceramic. Soc.*, **26**, 209, (1978).
30. H. Kinura, T. Masumoto, F.S. Spaepen, A.I. Taub in "Amorphous Metallic Alloys" p.187, Ed. F.E. Luborsky (Butterworths Monographs in Materials, London, 1984).
31. H.U. Kunzi, *Topics in Appl. Phys.*, **53**, 170, (1984).
32. J. Perez, F. Fouquet, G. Lormand in "Les Amorphes Metalliques" p.537 (CNRS Winter School, Aussois, France, 1983).
33. R. G. Vardiman, *Mat. Res. Soc. Symp. Proc.*, **27**, 699, (1984).
34. R. Hutchings, W.C. Oliver, *Wear*, **92**, 143, (1983).
35. J.B. Pethica, R. Hutchings, W.C. Oliver, *Nucl. Inst. Methods*, 209-210, 995, (1983).
36. J.C. Pivin, F. Pons, J. Takadoum, H.M. Pollock, *J. Mat. Sci.* **22**, 1087 (1987).
37. *Smithells Metals Reference Book*, Sixth Edition, Ed. E.A. Brandes, Butterworths (1983).
38. *Proc. Int. Ion Engineer, Cong.*, Ed. T. Takagi, Kyoto (1980).
39. A.P. Gerk, *J. Phys. D. : Appl. Phys.*, **9**, L179, (1976).
40. C.A. Brookes, *Phil. Mag.*, **A43**, 529, (1983).
41. D. Maugis, *Wear*, **62**, 349, (1980).

42. R.M. Hooper, C.A. Brookes, J. Mat. Sci., **19**, 4057, (1984).
43. M.G.S. Naylor, T.F. Page, J. Microscopy, **130**, 345, (1983).
44. C.C. Chen, A.A. Hendrickson in "The Science of Hardness Testing and Its Research Applications" p.274, Eds. J.H. Westbrook, H. Conrad, ASTM, Metals Park, Ohio.
45. A.P. Gerk, Phil. Mag., **32**, 355, (1975).
46. S.N.G. Chu, J.C.M. Li, J. Mat. Sci. **12**, 2200, (1977).
47. D. Tabor, "The hardness of metals", Clarendon Press, Oxford, 1951.
48. A.G. Atkins, A. Silverio, D. Tabor, J. Inst. of Metals, **94**, 369, (1966).
49. J.R. Matthews, Acta Met., **28**, 311, (1980).
50. H.J. Frost, M.F. Ashby, "Deformation Mechanism Maps", Pergamon, Oxford (1982).
51. C.B. Finch, O.B. Cavin, P.F. Becher, J. Crystal Growth **67**, 556, (1984).
52. J. Takadoum, J.C. Pivin, H.M. Pollock, J.D.J. Ross, H. Bernas, Nuclear Instruments and Methods, **B18**, 153, 1987.



KEY

- S - specimen
- P - pendulum assembly
- SR - specimen rotation facility and X-Y table
- MD - motor drive for tangential movement.
- AES - Auger electron spectrometer
- IG - Ion gun.
- FB - flexible bellows

Figure 1 : Ultra-high vacuum mechanical microprobe.

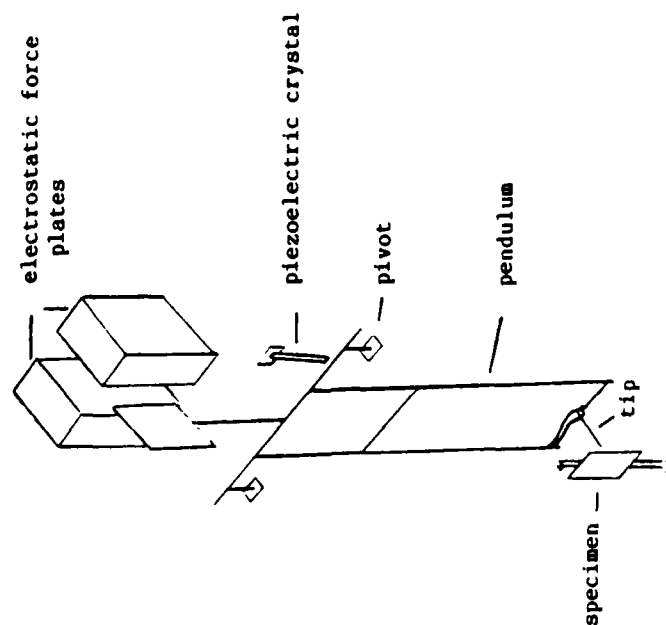


Fig. 2(a) : Tip assembly and loading device.

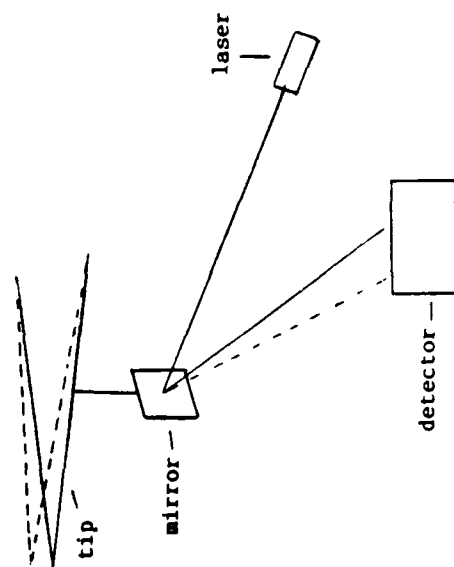


Fig. 2(b) : Method of friction force measurement using an optical lever.

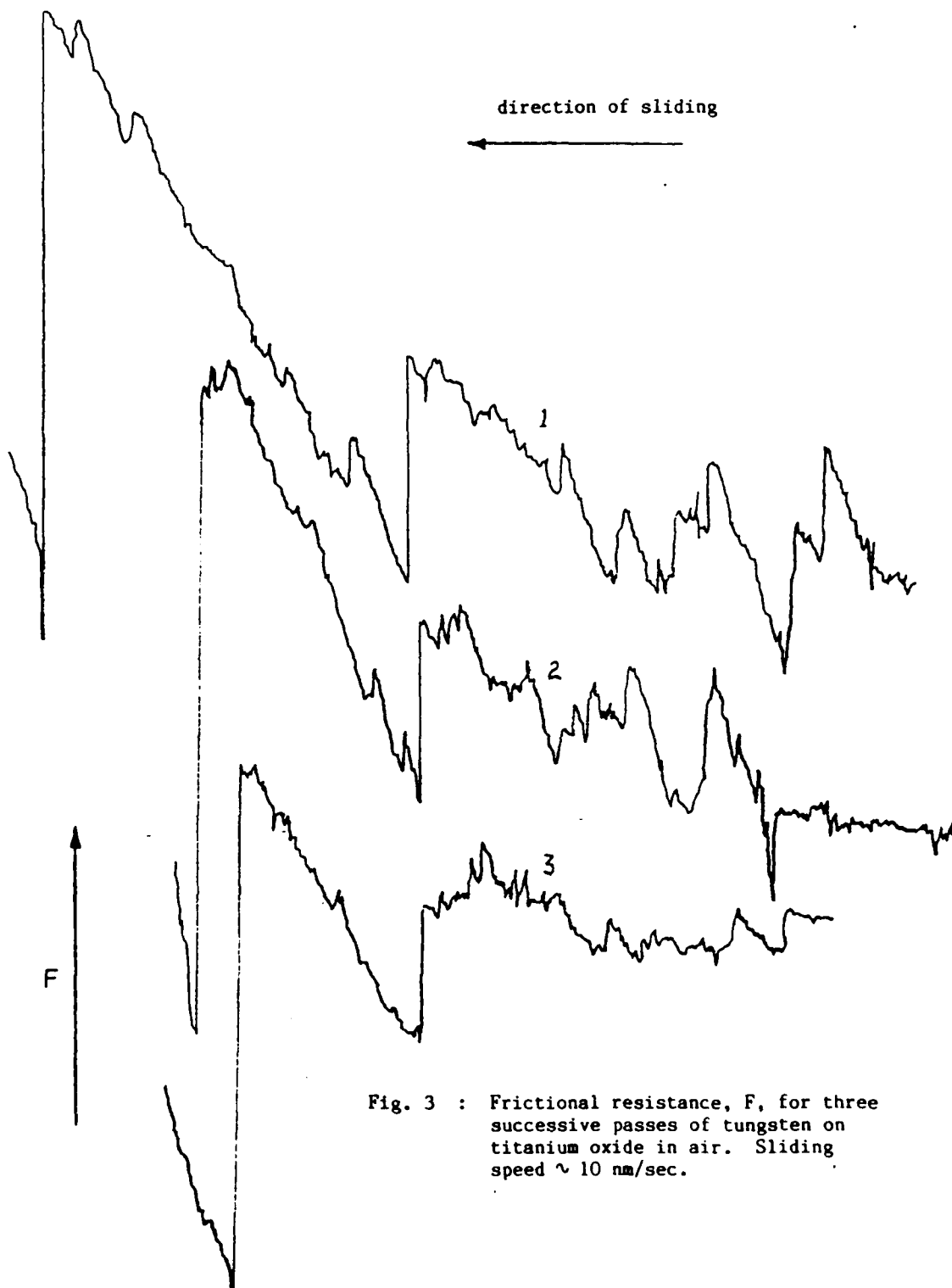


Fig. 3 : Frictional resistance, F , for three successive passes of tungsten on titanium oxide in air. Sliding speed ~ 10 nm/sec.

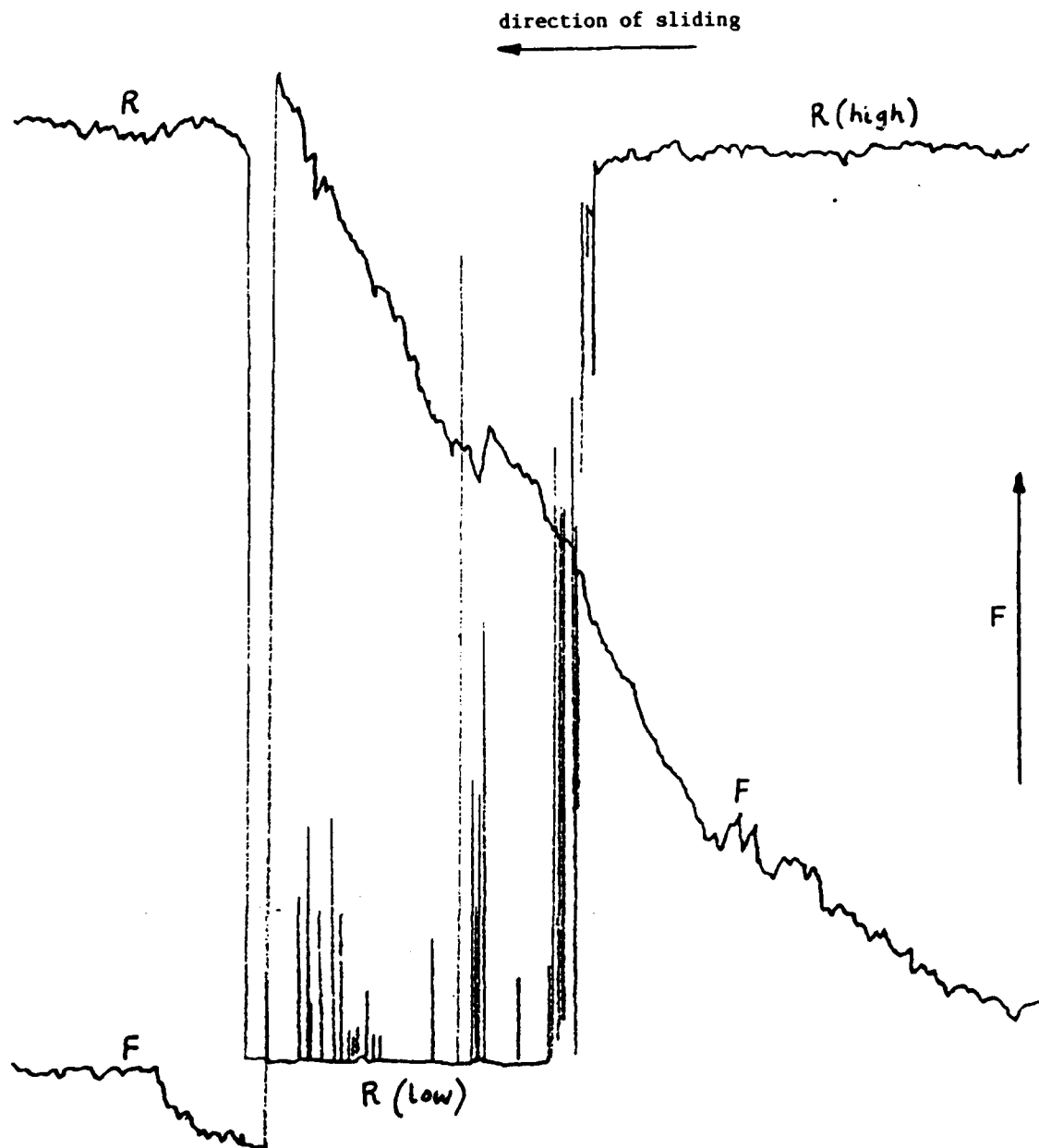


Fig. 4 : Friction force, F , plotted simultaneously with electrical resistance, R , for tungsten on titanium oxide in vacuum. Note the correlation between the drop in F (slip) and the abrupt increase in R towards the left of the figure.

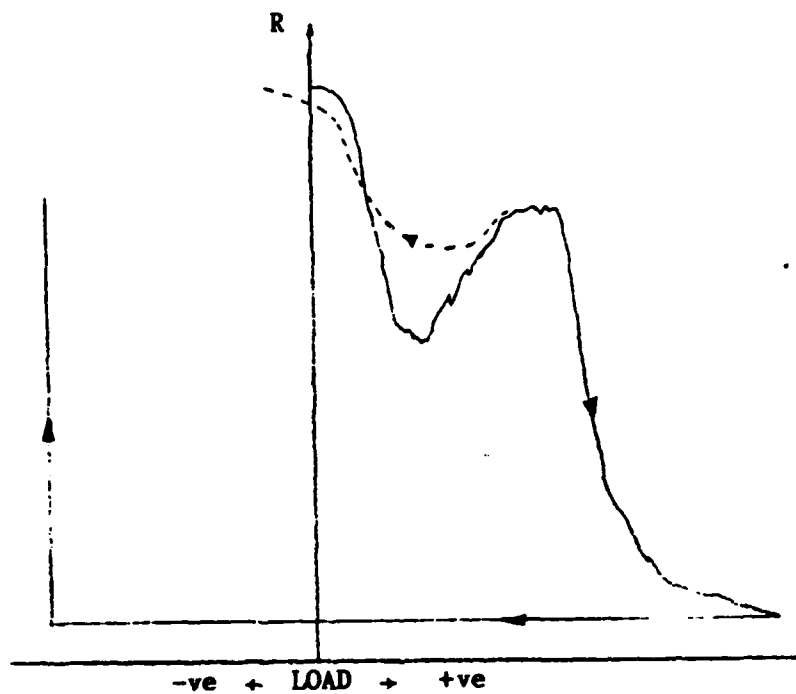


Fig. 5(a) : Loading and unloading plots for tungsten on titanium oxide after heating to $\sim 900^{\circ}\text{C}$.

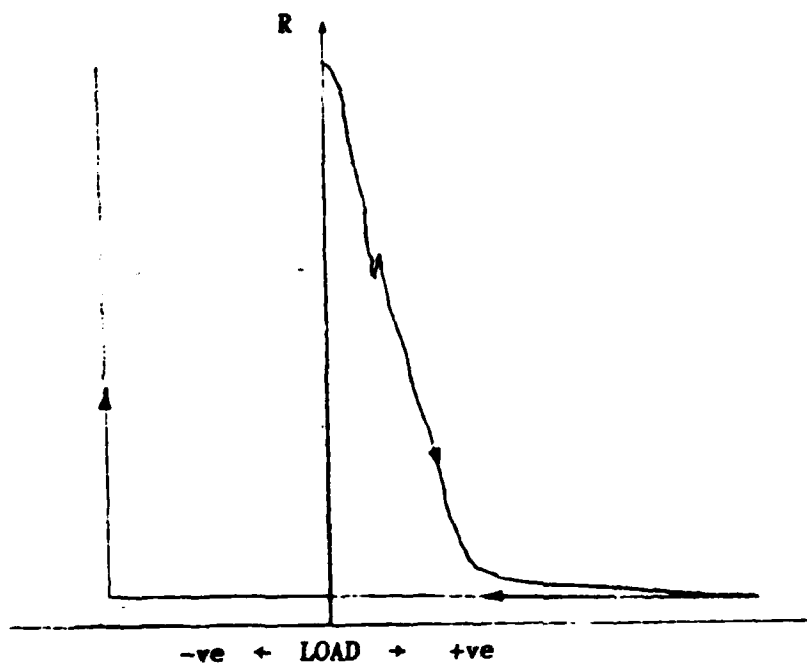


Fig. 5(b) : Loading and unloading plot for tungsten on titanium oxide after heating and ion erosion.

Table 1 : Implantation parameters for boron- and phosphorus- implanted nickel.

Ion	Energy (keV)	Dose /cm ²	R _p (nm)	ΔR _p (nm)	C(R _p) theor.	C(R _p) exper.	Amorphous fraction at R _p
B	50	1.10 ¹⁶	61	23	1.9.10 ⁻¹	1.5.10 ⁻²	5.10 ⁻²
		5.10 ¹⁶			9.5.10 ⁻²	7.2.10 ⁻²	2.0.10 ⁻²
		1.10 ¹⁷			1.9.10 ⁻¹	1.4.10 ⁻¹	5.0.10 ⁻¹
		2.10 ¹⁷			3.8.10 ⁻¹	2.8.10 ⁻¹	9.0.10 ⁻¹
		3.10 ¹⁷			5.7.10 ⁻¹	4.1.10 ⁻¹	1.0
P	125	1.10 ¹⁶	53	24	1.8.10 ⁻²	1.4.10 ⁻²	3.10 ⁻²
		5.10 ¹⁶			9.1.10 ⁻²	8.10 ⁻²	2.2.10 ⁻¹
		1.10 ¹⁷			1.8.10 ⁻¹	1.2.10 ⁻¹	5.10 ⁻¹
		2.5.10 ¹⁷			4.5.10 ⁻¹	2.4.10 ⁻¹	1.0
B	180	5.6.10 ¹⁷	240		2.5.10 ⁻¹	2.5.10 ⁻¹	1
	70	2.4.10 ¹⁷	110		3.1.10 ⁻¹		
	20	8.5.10 ¹⁶	30		2.9.10 ⁻¹		
		same × 9/10			same × 9/10	2.2.10 ⁻¹	1
		same × 2/3			same × 2/3	1.6.10 ⁻¹	8.0.10 ⁻¹
		same × 1/3			same × 1/3	8.0.10 ⁻²	2.0.10 ⁻¹
		same × 1/10			same × 1/10	2.5.10 ⁻²	0
		same × 2/100			same × 2/100	5.0.10 ⁻³	0

Table 2 : Numerical data for implanted and electroless nickel.

Alloy	$I_p/(I_p)_{Ni}^*$ (measured here)	$H_v/(H_v)_{Ni}^*$ (from literature)	R (%)	I_p/R (GPa)	$E/(1-\nu^2)^{**}$ (GPa) (from literature)
Ni	1	1	4.5±0.5	160	220 [28]
Multi-energy implants:					
Ni-0.5%B	1.6±.2		5±0.5	240	
Ni-2.5%B	3.2±.2		8±1	300	
Ni-8%B	3.7±.3		10±1	270	
Ni-16%B	4.5±.2		15±2	220	
Ni-22%B	4.7±.2		15±2	230	
Ni-25%B	4.7±.2		15±2	230	
Ni-25%B relaxed	5.9±.3		15±2	290	
Ni-25%B crystallised	5.3±.3		15±2	260	
Ni-3%Belec- troless	3.8±.3	2.80±.03	8.5±1	330	
Ni-14%Belec- troless	4.7±.3	2.94±.03	13±1	260	
Ni-25%Belec- troless	4.9±.3	3.21±.03	3.5±.1 [28]	15±1	240
Ni-25%Belec- troless, crystallised			4.9±.4 [28]		
Ni ₃ B, single crystal			5.0±.2 [51]		200 [51]
Ni-(15-20%B), (0-5%Si) metglass			4.1±.1 [30-32]		120 to 180 [30-32]
(Fe,Ni,Co,Cr)-(15-20%B)- (0-5%Si) metglass			3.4-5.0 [30-32]		
Ni-17.4%P electroless	4.1±.3	2.90±.02	15±1	200	
Ni-20%P metglass			2.9±.2 [30-32]		130 [30-32]

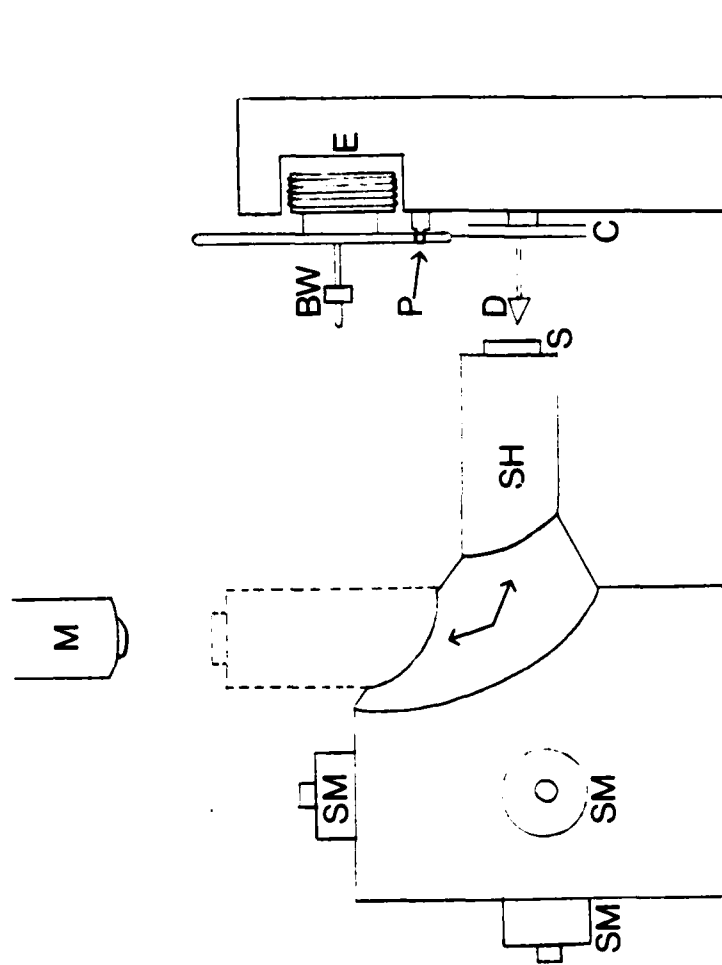
*using measured values for nickel of $I_p = 7.3 \pm 0.5$ GPa and $H = 2.21 \pm 0.05$ GPa.

**assuming ν -values of 0.315 for Ni and 0.39 ± 0.03 for metglasses and Ni₃B single crystals [30,31,32,28,51]

Table 3: measured doses and concentrations for
nitrogen-implanted titanium.

Nominal N dose ($\times 10^{15}$ atoms/cm ²)	Measured total amounts in the film ($\times 10^{15}$ atoms/cm ²)				Mean N stoichiometry	TiO ₂ thickness (nm)
	N	O	C	Ti		
0	10±2	38±12	10±2	2645±10		6±2
46	63	16	5	2664	Ti _{0.98} N _{0.02}	3
282	279	30	5	2515	Ti _{0.90} N _{0.10}	5
554	579	62	7	2403	Ti _{0.81} N _{0.19}	10
720	730	70	16	2317	Ti _{0.76} N _{0.24}	11
930	1050	110	20	2159	Ti _{0.67} N _{0.33}	17
1380	1593	48	8	2027	Ti _{0.56} N _{0.44}	8

Nominal concentrations (%)	Mean N concentration (%)		Depth of maxima (nm)		N concentration extremes (%)			
	20-470nm	40-60nm	R.B.S.	S.I.M.S.	R.B.S.		S.I.M.S.	
					max	min	max	min
1.7	1.7	1.5		80 285			1.7 1.9	1.3
10.3	10.0	8.5		95 290			10 11	7.5
20.3	19.4	17	80 230 350	105 195 360	20 25 20	15 17	19 17 18	15 16
26.4	24.0	20	55 230 360	55 150 360	26 28 24	18 22	22 28 22	18 21
34.1	32.7	29	80 250 410	75 240 385	32 37 39	30 30	39 37 33	35 31
50.5	44.0	40	60 230 405	65 220 410	40 45 44	35 40	47 47 44	35 38



KEY

S	specimen
SH	specimen holder
D	diamond indenter
C	capacitor plates
E	electromagnet
P	pivot
BW	balance weight
M	microscope
SM	stepping motor

Figure 1 : Sub-micron indentation device

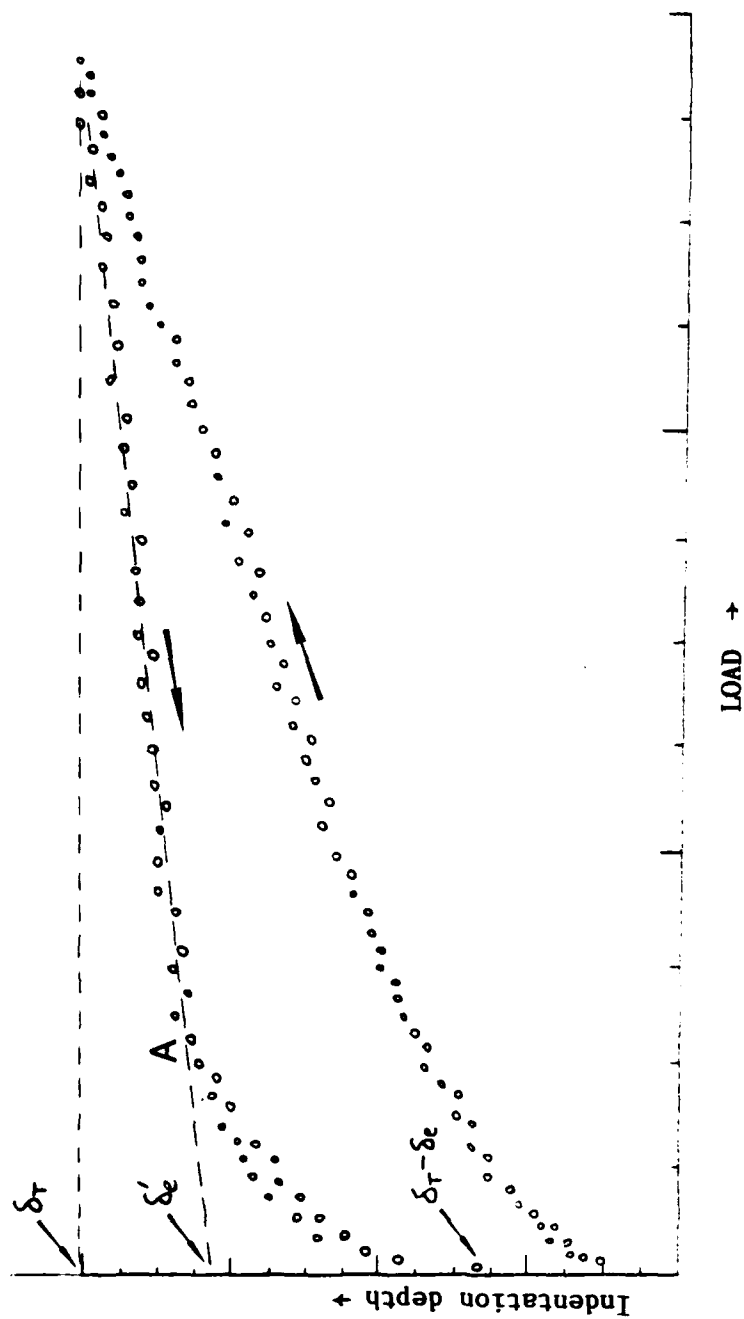


Figure 2 : Typical depth/load test showing loading (+) and unloading (o) curves and the relevant notation (see text).

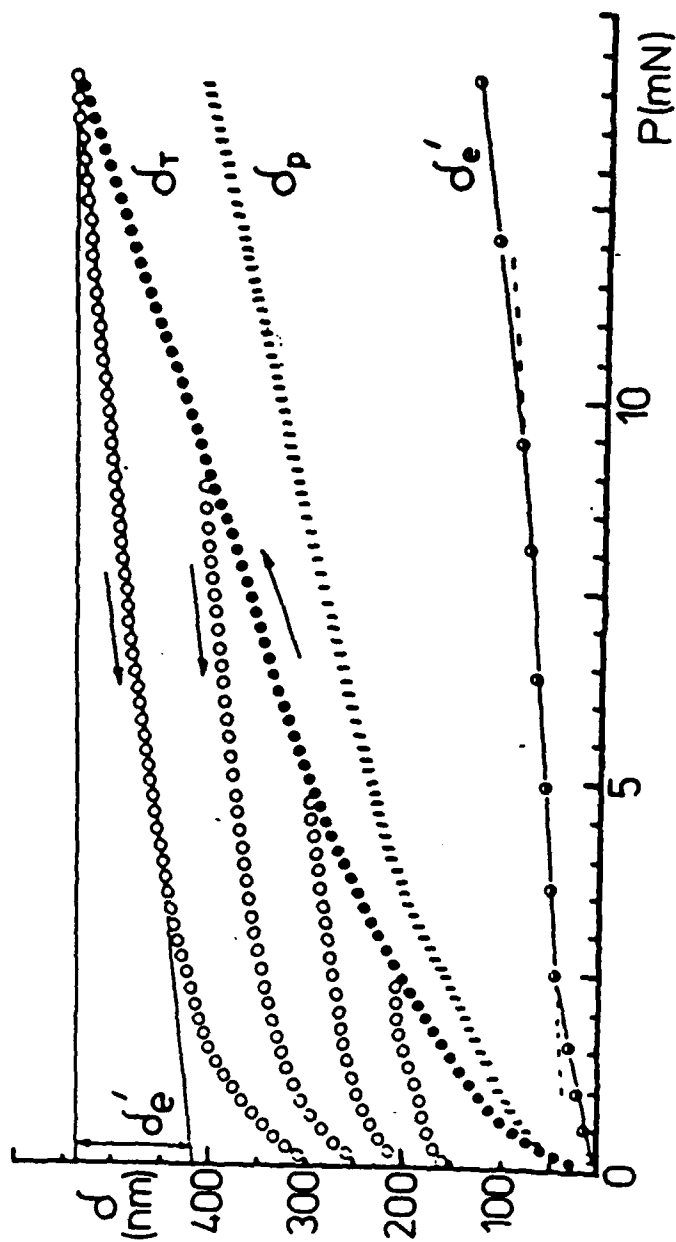


Fig.3: Raw loading (\bullet) and unloading (\circ) curves $\delta_r = f(P)$ obtained for a 150-nm thick Ni film. δ_e' and δ_p are defined in the text. The scatter of data around the averaged δ_p -value being less than 5 nm, error bars have not been shown here.

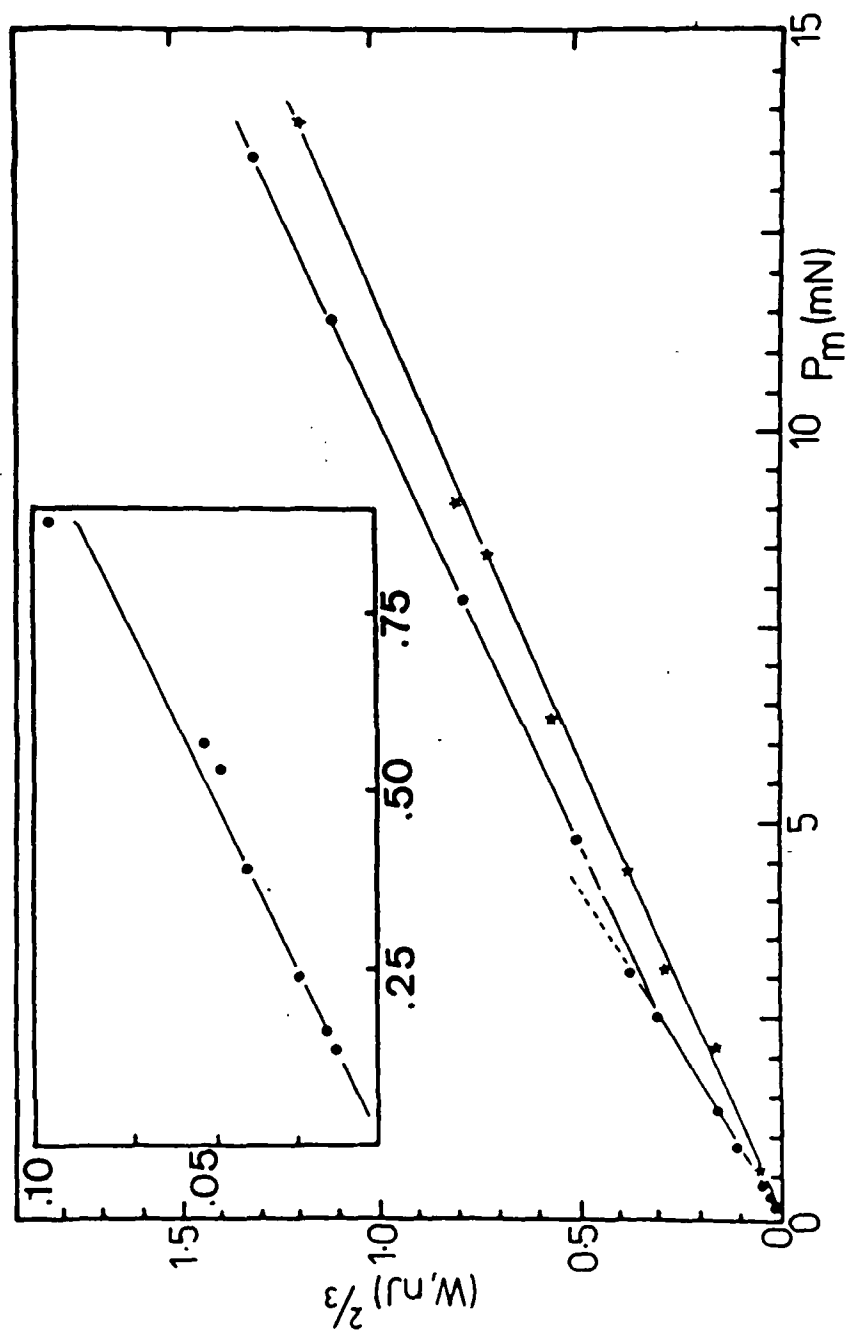


Fig.4: Variation of hysteresis area W with the maximum load applied in each test, for a 150-nm thick nickel film(\bullet) and for the silicon substrate(\star). The insert shows data obtained at loads below 1 mN.

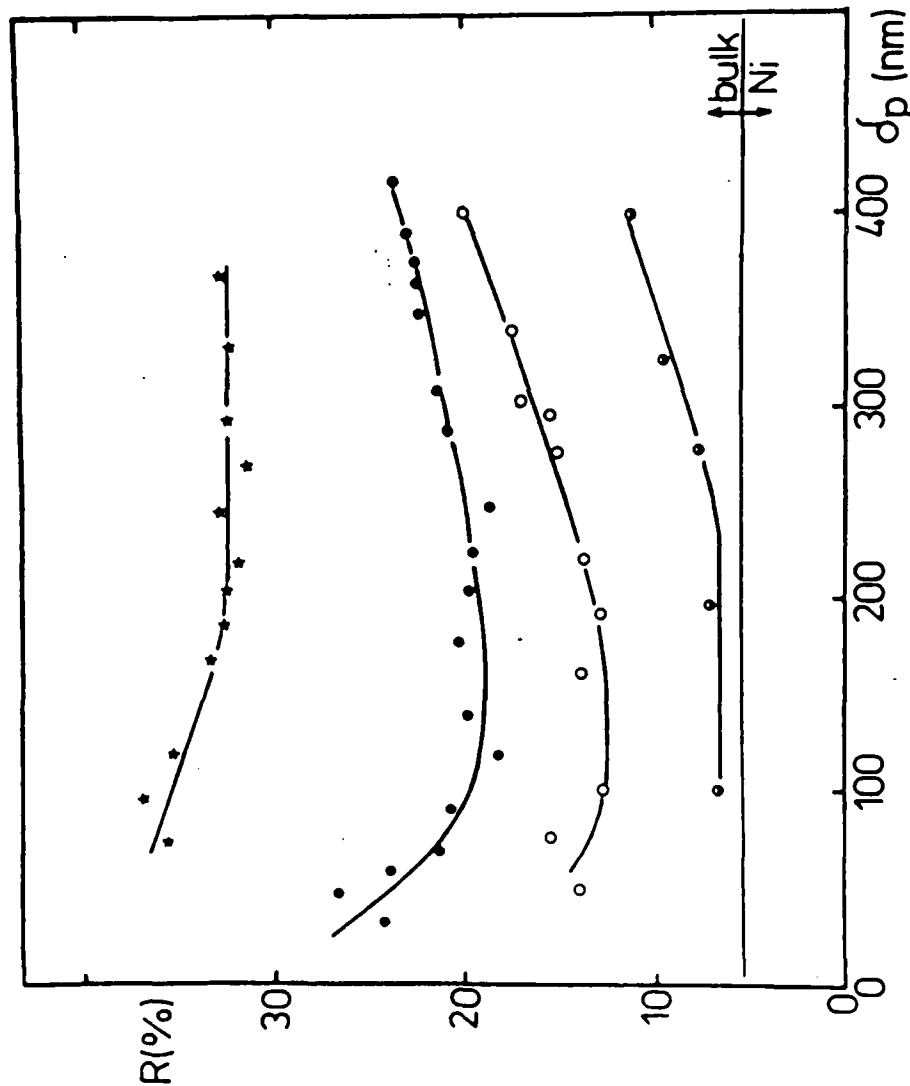


Fig.5: Variation of the elastic recovery parameter R with the plastic indentation depth (δ_p) of the test, for the silicon substrate (★), and for Ni films of thickness 150 nm (●), 300 nm (○), and 600 nm (○). The constant value of R obtained for bulk polycrystalline

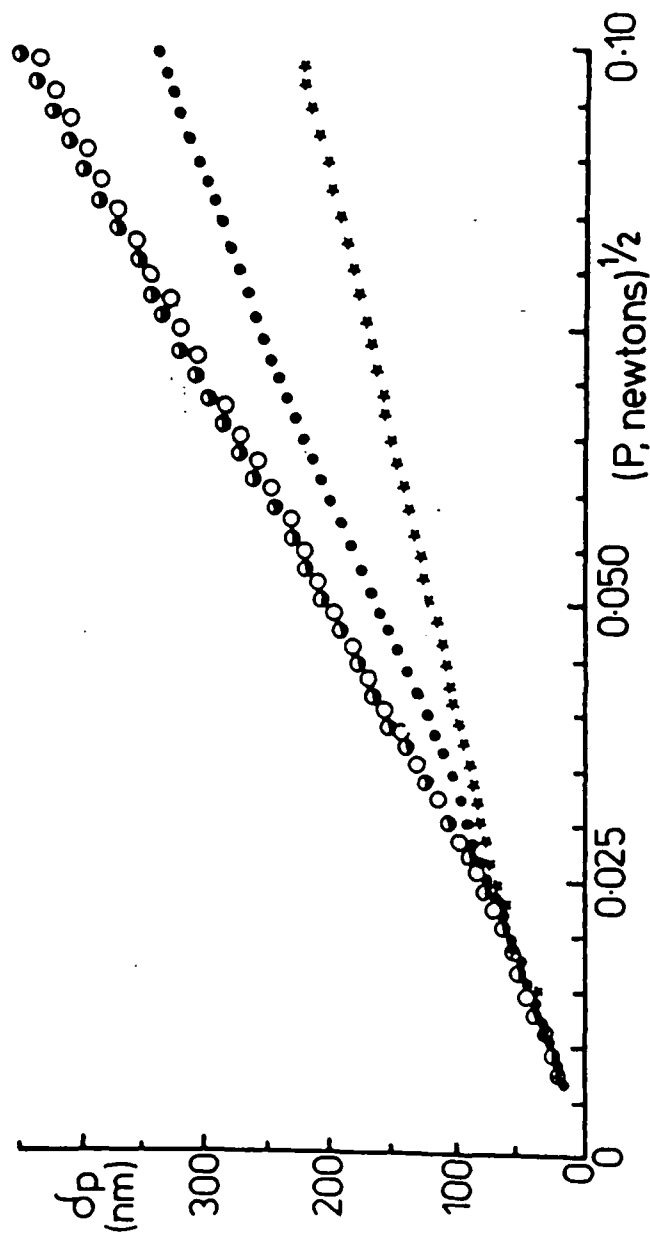


Fig 6: Variation of the off-load depth d_p with $P^{1/2}$, for silicon (★) and for nickel films of thickness 150 nm (●), 300 nm (○), and 600 nm (○). Each point represents the mean of typically five to ten data points, obtained from tests on at least six different areas.

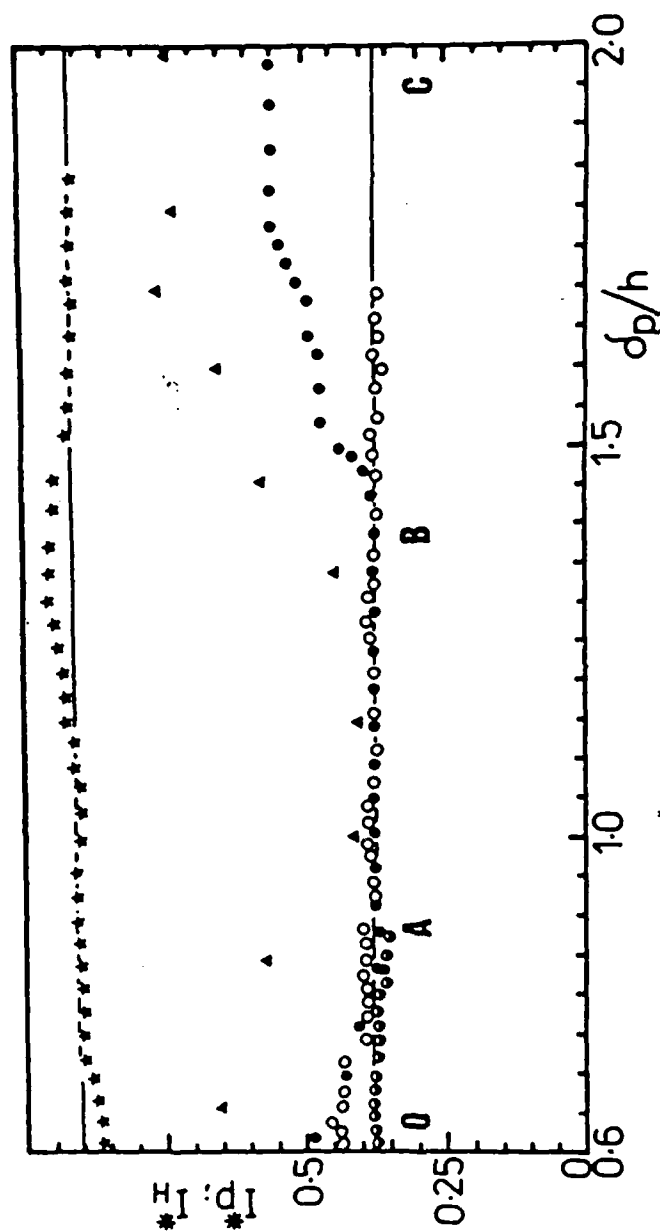


Fig. 7: Variation of I_p^* with the ratio δ_p/h for silicon (★) and for nickel films of thickness 150 nm (○), 300 nm (△), and 600 nm (◻). (▲) shows I_H^* for the 150-nm film. All uncertainties are less than 0.02.

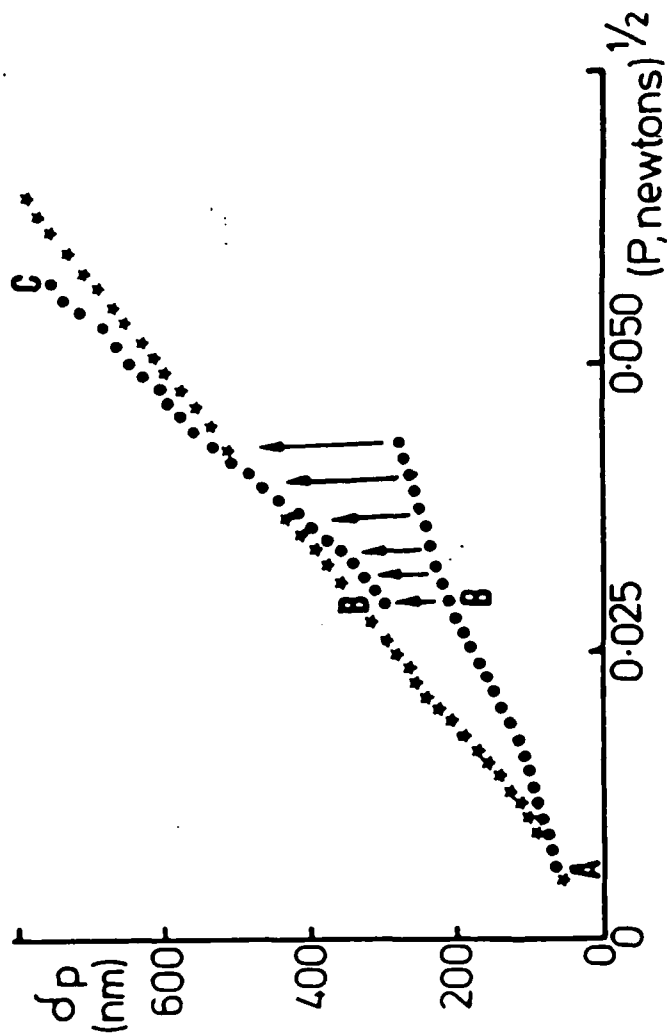


Fig. 8: Average δp -values as a function of $p^{1/2}$ for a 266-nm thick Nb_2O_5 film grown on polycrystalline Nb (dots; stars show data for substrate alone). Vertical arrows show points B at which jumps in the indented depth were observed in different tests.

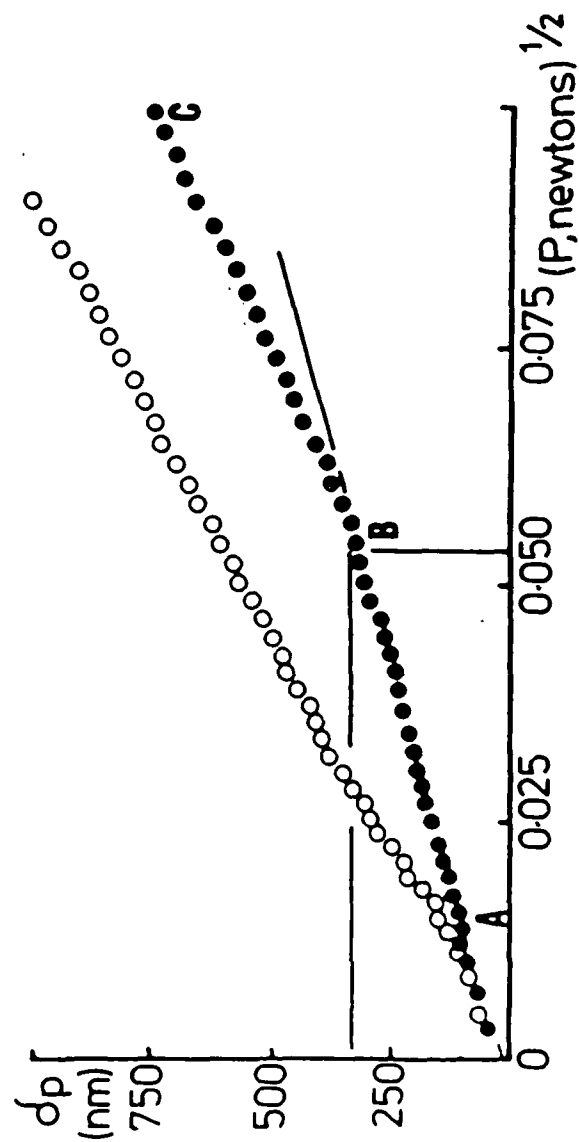


Fig.9: Averaged δ_p -values as a function of $P^{1/2}$ for (○) non-implanted polycrystalline Ni and (●) a Ni-25% B implanted layer. The scatter of data around the averaged δ_p -values was always less than 10 nm.

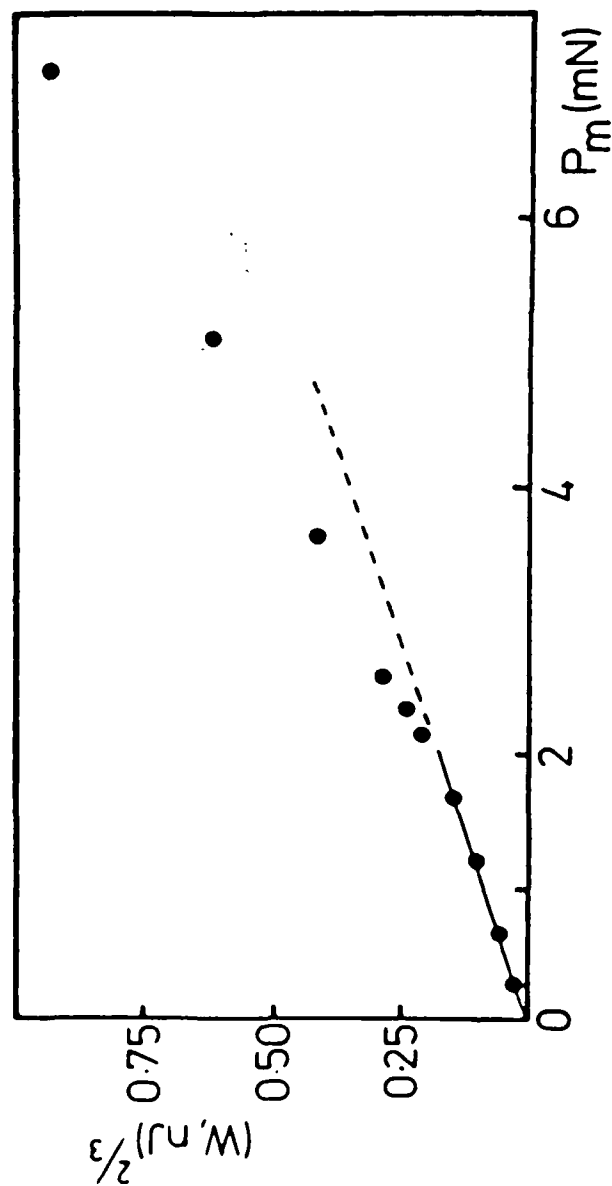


Fig.10 : Variation of hysteresis area W with maximum load for the Ni-25% B implanted layer.

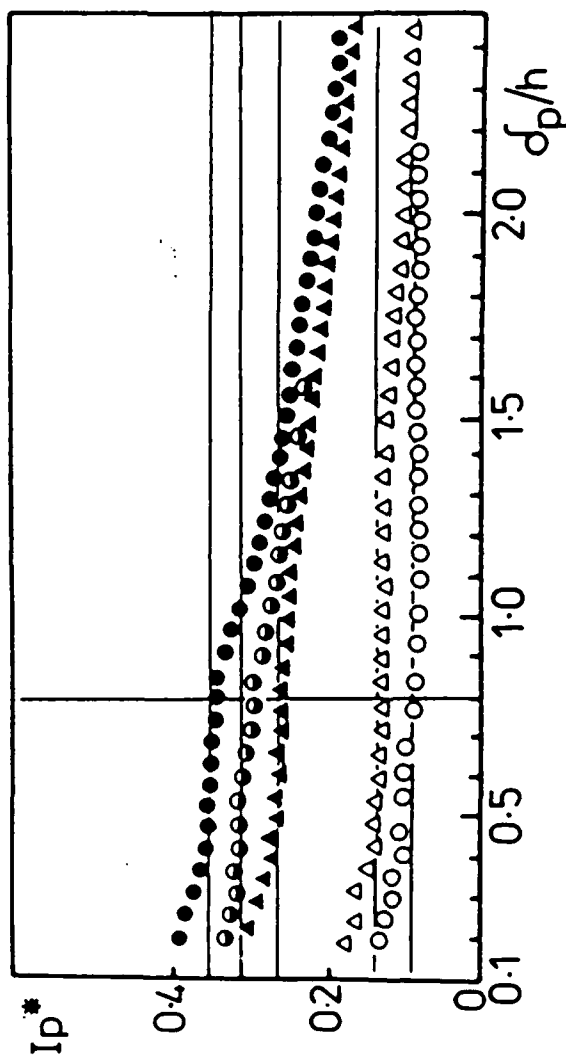


Fig.11 : Variation of I_p^* with the ratio δ_p/h for (o) non-implanted Ni, and (Δ) Ni-0.5% B, (\triangle) Ni-2.5% B, (\bullet) Ni-8% B, (\circ) Ni-16% B and Ni-25% B implanted films. Error bars on I_p^* are 0.05 at δ -values below 100 nm and 0.02 nm thereafter.

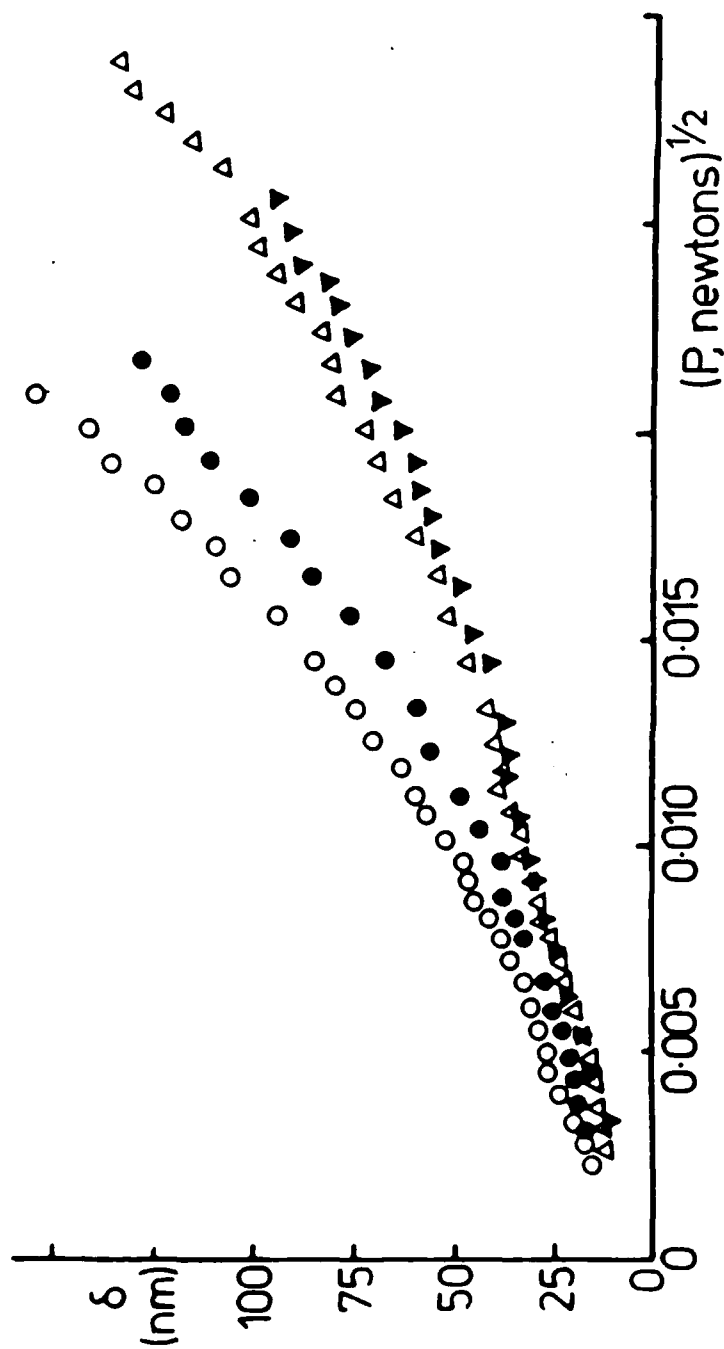


Fig. 12: On-load indentation depth δ as a function of $(\text{load}, P)^{1/2}$, for unimplanted nickel (○) and for surfaces implanted at doses of (●) 10^{16} B, (Δ) 10^{17} B, (∇) 2 to 3×10^{17} B $\cdot \text{cm}^{-2}$ at a single energy of 50 keV. Here and in other figures unless otherwise stated, each point represents the mean of typically five to fifty data points, obtained from tests on at least six different areas. The standard error for each point was always less than 10 nm.

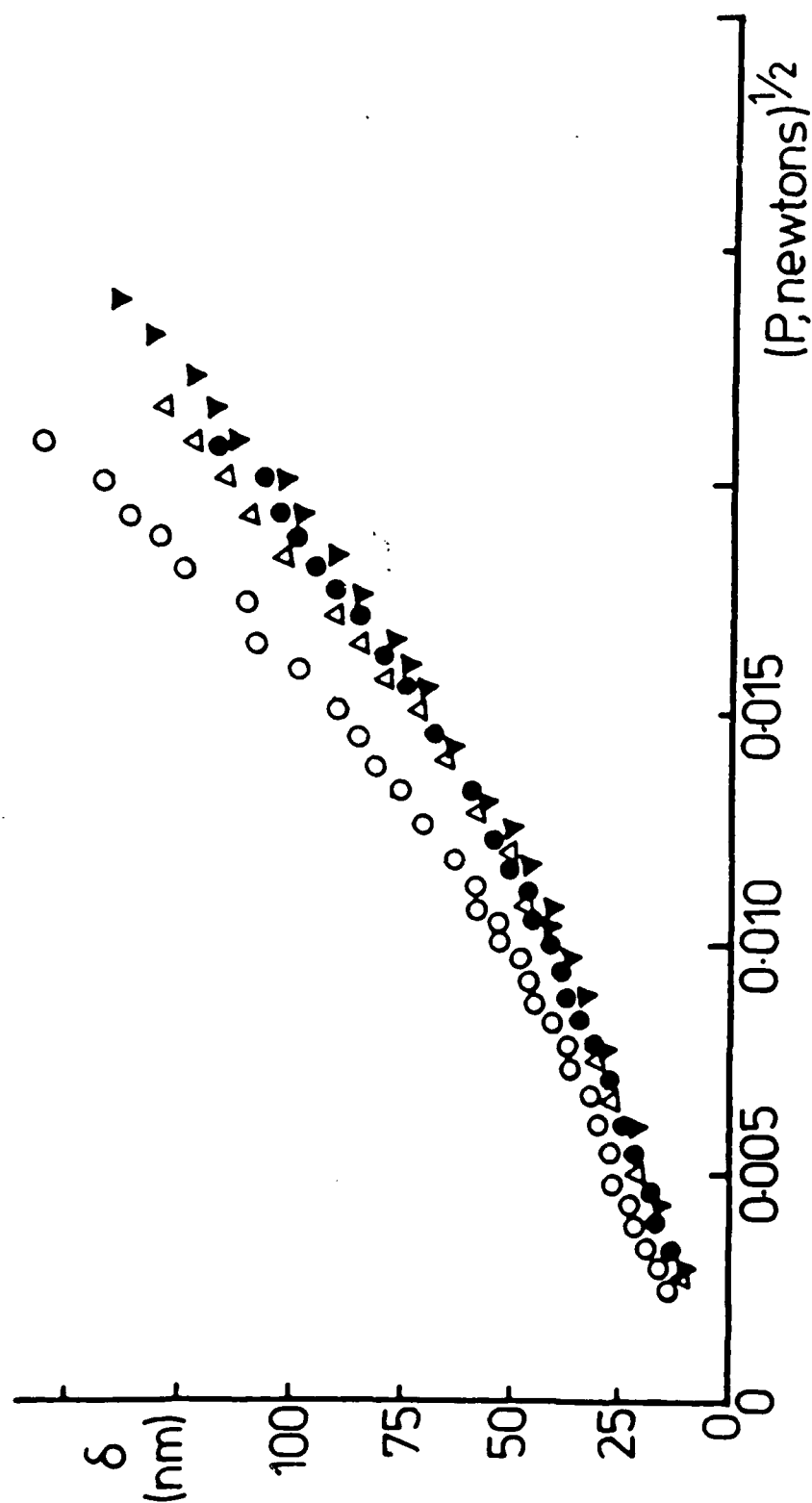


Fig. 13: 0n-load indentation depth δ as a function of $(\text{load}, P)^{1/2}$, for unimplanted nickel (○) and for surfaces implanted at doses of (\bullet) 10^{16} P, (Δ) 10^{17} P, (∇) 2.5×10^{17} P $\cdot \text{cm}^{-2}$ at a single energy of 125 keV. The different doses produce an almost identical effect.

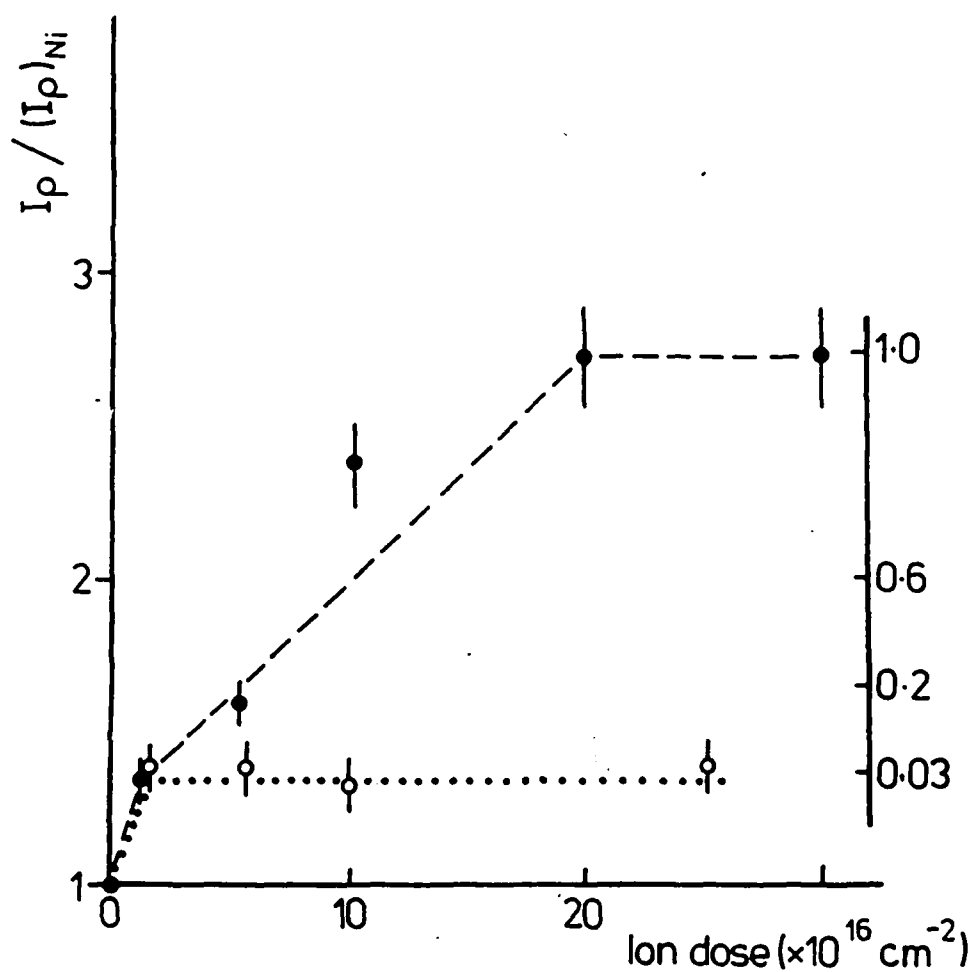


Fig. 14 : Left-hand ordinate: Variation of on-load plasticity index I_p with implanted dose of (●) boron, (○) phosphorus (single energy: calculated at $\delta = 60 \text{ nm}$ and normalised with respect to pure nickel). Right-hand ordinate: (non-linear scale or shown, pectral line).variation in the amorphous fraction with the ion dose. The dotted line (arbitrary scale) indicates the variation in disorder of the residual crystal [24, 25, 27].

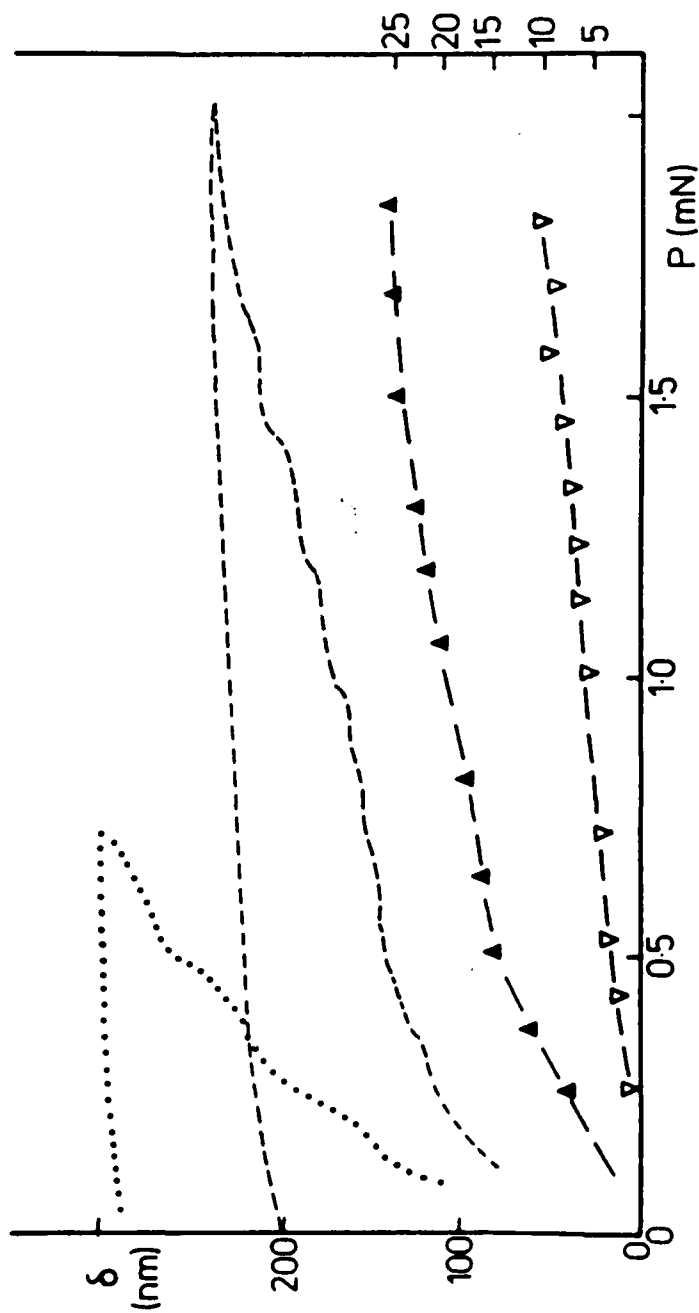


Fig. 15: Left-hand ordinate: raw loading and unloading curves for (dots) unimplanted Ni, (dashes) Ni-25% B implanted film, multi-energy, thickness 300 nm. Right-hand ordinate: δ_e' derived from unloading curves at various maximum loads, for (▽) Ni, (Δ) Ni-25% B (these data cannot be compared directly with those of figures 3-5, as a different indenter was used).

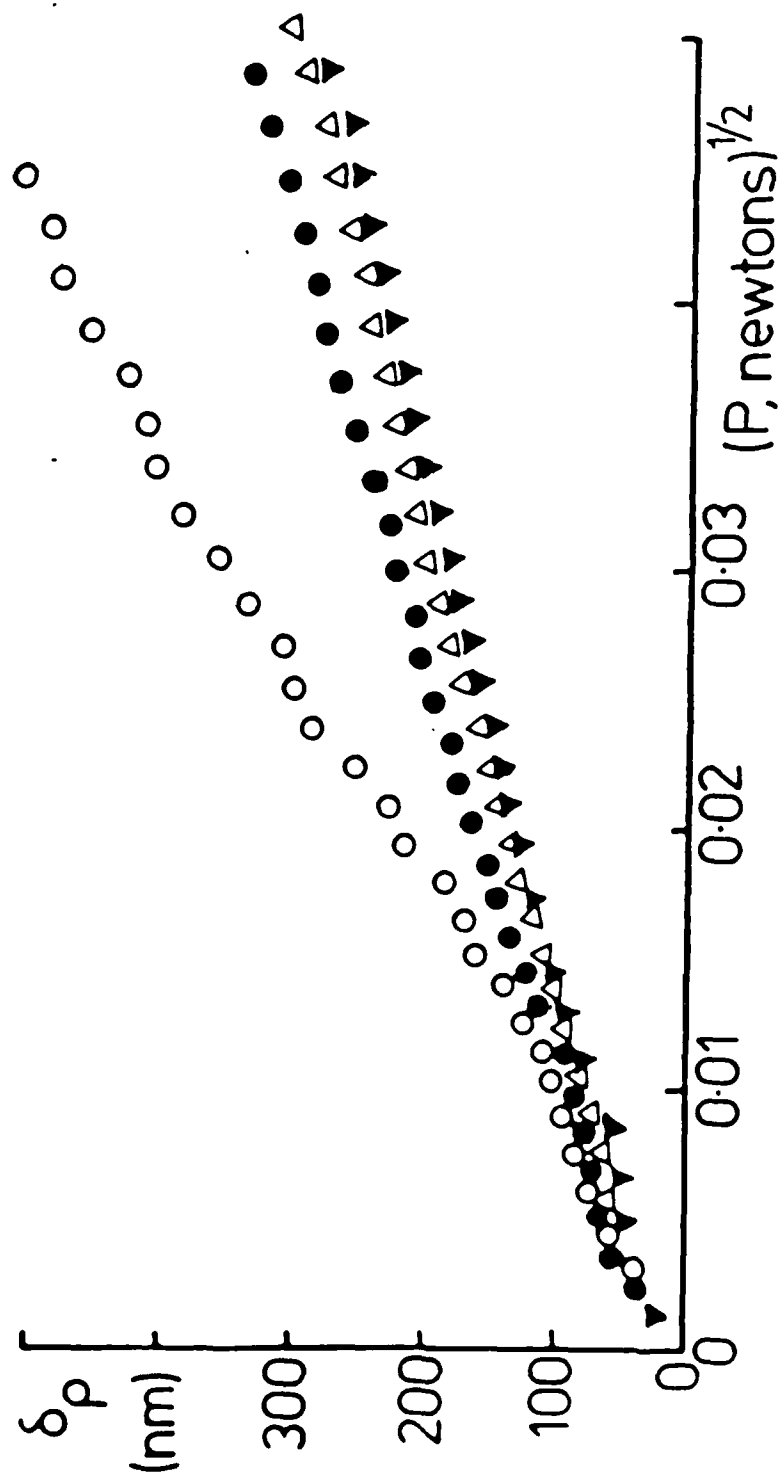


Fig. 16 : Off-load indentation depth δ_p as a function of $P^{1/2}$ for (○) unimplanted Ni, (●) Ni-2.5%B, (△) Ni-8%B, (▼) Ni-16 and 25%B multi-energy implanted films.

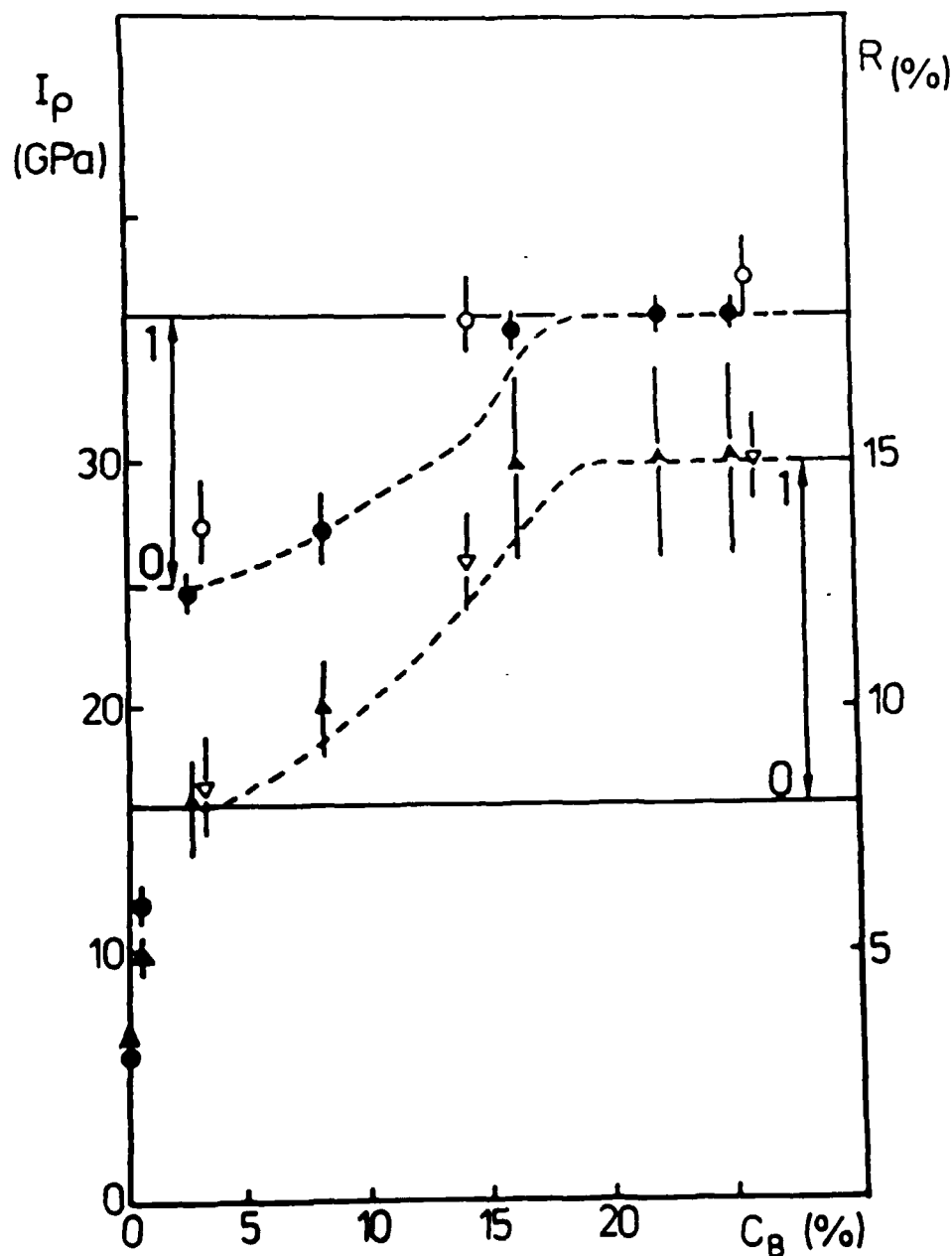


Fig. 17 : Dose-variation of off-load plasticity index (circles) and of elastic recovery index (triangles), for 300 nm-thick Ni-B multi-energy implanted film (full symbols) and for Ni-B electroless films (open symbols). Data from Fig. 7, calculated at a depth of 240 nm (variation with depth is presented in ref. [18]). Pecked lines indicate increase in the amorphous fraction, from 0 to 1 (linear scale). All data are directly related to the X-scale only, so that the relative positioning of the various vertical axes is not significant.

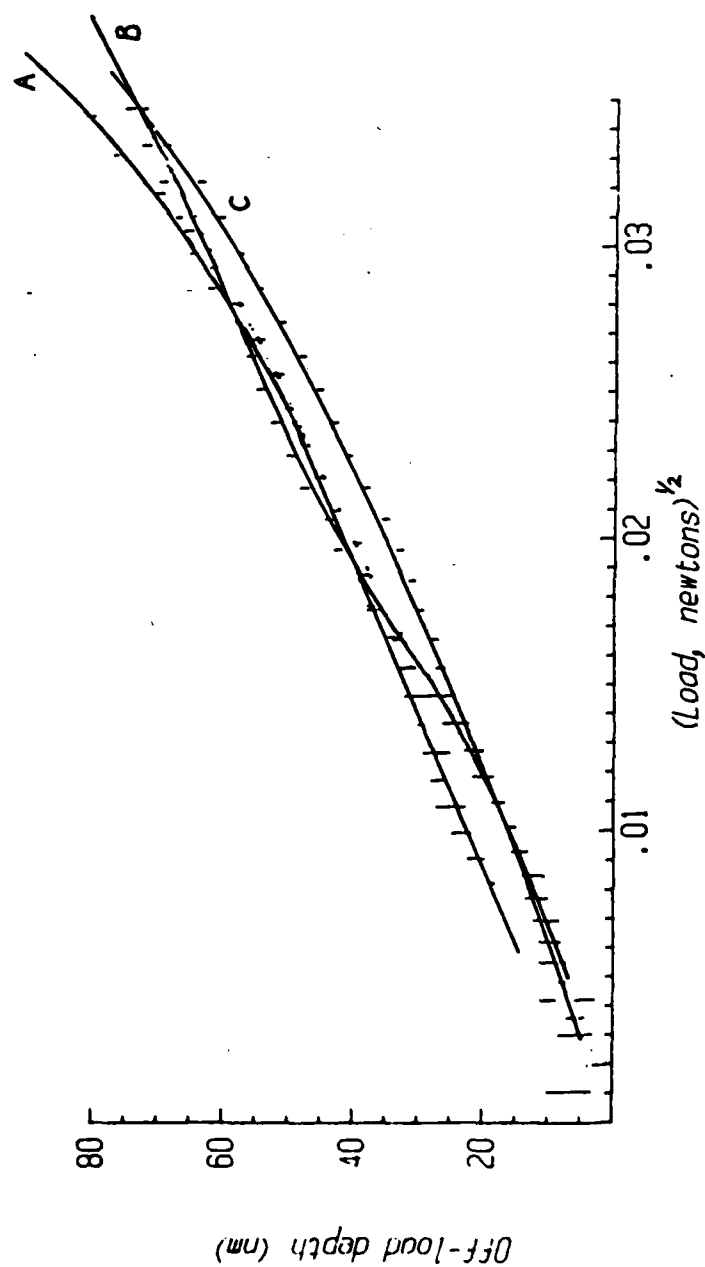


Fig. 18 : Off-load indentation depth as a function of square root of load at small depths for : amorphous Ni-25%B of thickness 120 nm (curve A), amorphous Ni-25%B of thickness 300 nm (curve B) and amorphized Ni₃B (curve C). Each bar indicates limits of error for typically five to fifty data points, obtained from tests on at least six different areas.

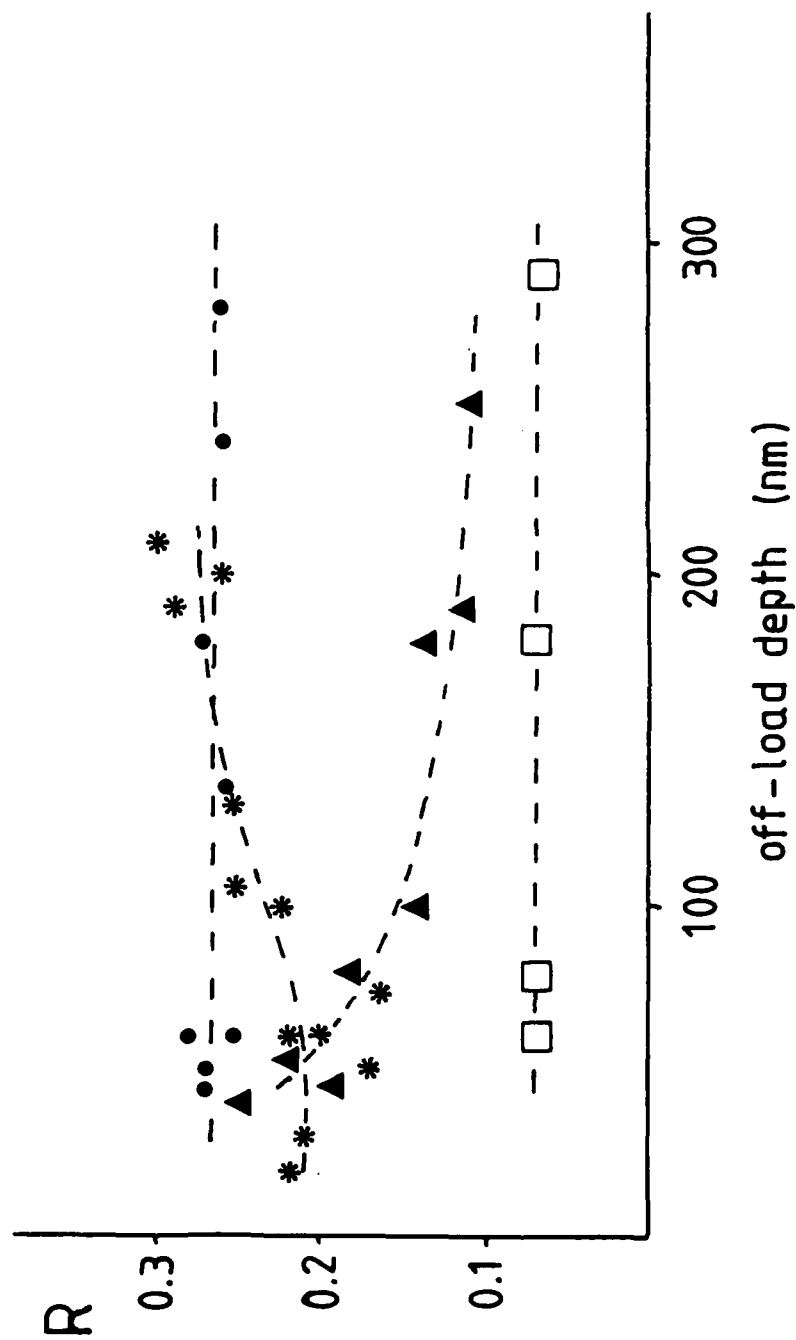


Fig. 19 : Elastic recovery parameter as a function of indentation depth for:
 single-crystal Ni_3B (o), amorphous Ni-25Zr (Δ), amorphized Ni_3B (*),
 polycrystalline nickel (\square).

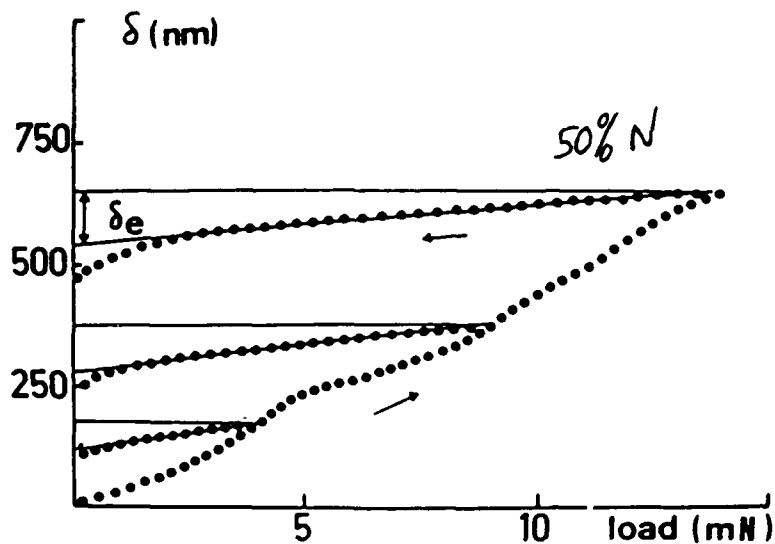


Fig. 20 : Raw indentation loading (+) and unloading (+) curves with different maximum loads recorded on Ti-50% N.

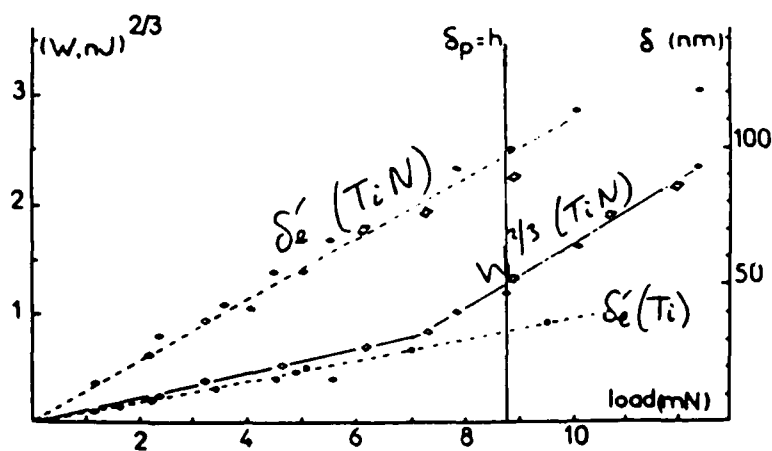


Fig. 21 : $W^{2/3}$ (—) and δ_e (----) as a function of load for unimplanted Ti (●), Ti implanted with 34% N (◊) and Ti implanted with 50% (◆).

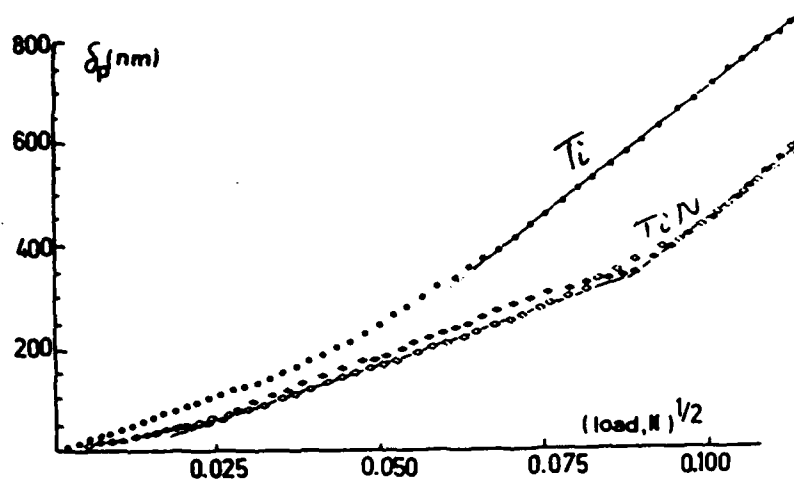


Fig. 22 : Plastic indentation depth as a function of square root of load for the same films as in fig. 12.

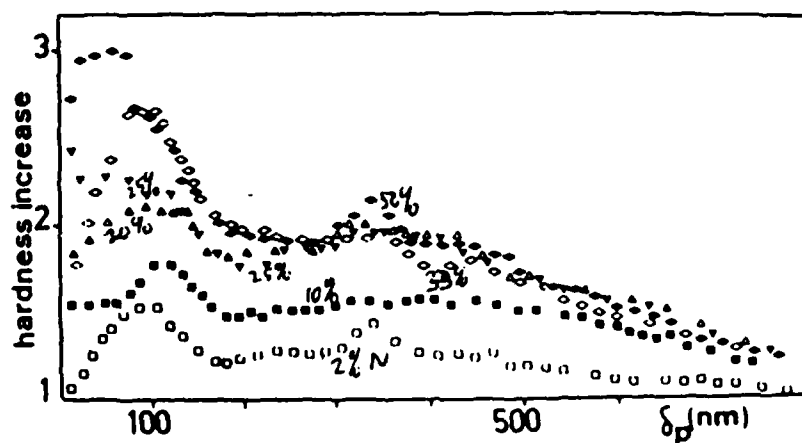


Fig. 23 : Hardness increase with respect to pure Ti as a function of plastic indentation depth. (□) Ti-2%Ni; (■) Ti-10%Ni, (Δ) Ti-20%Ni (▼) Ti-25%Ni; (◇) Ti-33%Ni; (◆) Ti-50%Ni.

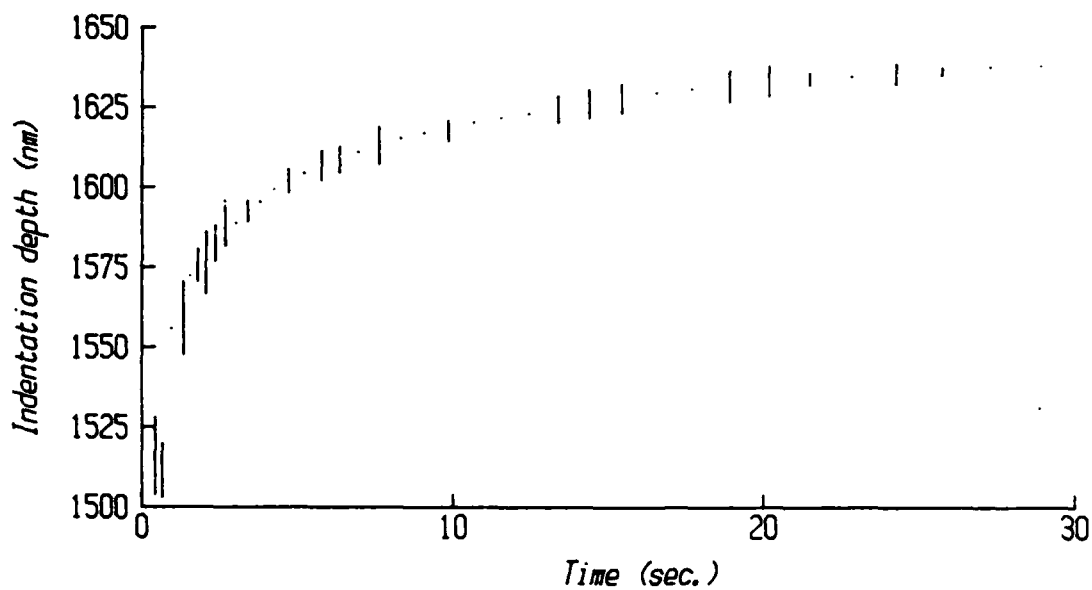


Fig. 24(a) : Time-dependent data for polyethylene terephthalate (P.E.T.)
at a load of 2.35 mN.

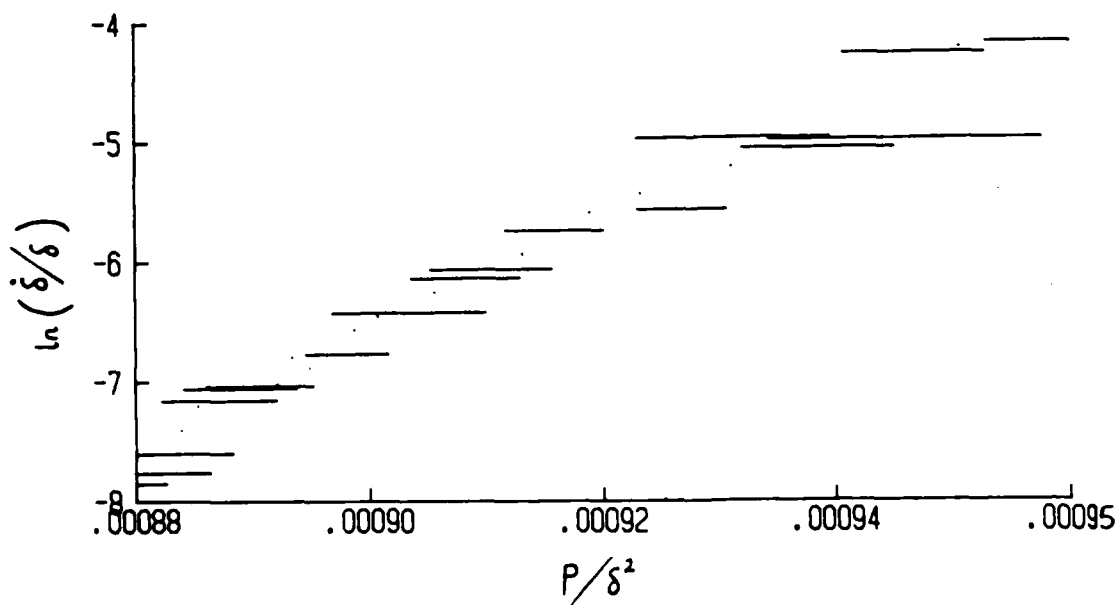


Fig. 24(b) : "Viscosity" curve (equivalent strain as a function of stress)
for P.E.T.

END

9-87

DTIC